Encapsulation of noble metal nanoparticles through seeded emulsion polymerization as highly stable plasmonic systems

Encapsulation of Noble Metal Nanoparticles through Seeded Emulsion Polymerization as Highly Stable Plasmonic Systems

Leonardo Scarabelli[1,2,†,*], Marius Schumacher[3,†], Dorleta Jimenez de Aberasturi[1], Jan-Philip Merkl[3], Malou Henriksen-Lacey[1], Thais Milagres de Oliveira[4], Marcus Janschel[3], Christian Schmidtke[3], Sara Bals[4], Horst Weller[3,*], and Luis M. Liz-Marzán[1,5*]

[1]CIC biomaGUNE and CIBER-BBN, Paseo de Miramón 182, 20014 Donostia-San Sebastián, Spain
[2]Department of Chemistry & Biochemistry, University of California Los Angeles, Los Angeles, California 90095 USA
[3]Institute of Physical Chemistry, University of Hamburg, 20146 Hamburg, Germany
[4]Electron Microscopy for Materials Science (EMAT), University of Antwerp, Groenenborgerlaan 171, 2020 Antwerp, Belgium
[5]Ikerbasque, Basque Foundation for Science, 48013 Bilbao, Spain

† These authors contributed equally
*Corresponding authors: lscarabelli@ucla.edu (LS); weller@chemie.uni-hamburg.de (HW); llizmarzan@cicbiomagune.es (LMLM)

Abstract

The implementation of plasmonic nanoparticles *in vivo* remains hindered by important limitations such as biocompatibility, solubility in biological fluids, and physiological stability. We present herein a general and versatile protocol, based on seeded emulsion polymerization, for the controlled encapsulation of gold and silver nanoparticles. Our procedure enables the encapsulation of single nanoparticles as well as nanoparticle clusters inside a protecting polymer shell. Specifically, we demonstrate the efficient coating of nanoparticles of both metals, with final dimensions ranging between 50 and 200 nm, *i.e.* sizes of interest for bio-applications. Such hybrid nanocomposites display extraordinary stability in high ionic strength and oxidizing environments, along with high cellular uptake, and low cytotoxicity. Overall, the prepared nanostructures are promising candidates for plasmonic applications under biologically relevant conditions.

Introduction

The unique interaction of metal nanoparticles with light opens up unexplored avenues for the development of alternative approaches in bioimaging and diagnostics.[1–4] In fact, nanomedicine represents one of the most promising research areas for application of plasmonic nanoparticles,[5,6] related to drug-delivery,[7] photothermal therapy,[8] antibacterial surfaces,[9,10] theranostics,[11,12] and biosensing.[13,14]

Taking full advantage of the plasmon-engineering capabilities offered by state-of-the-art colloidal synthetic methods,[15] both gold and silver nanoparticles have been implemented as bioimaging probes,[3] exploiting different spectroscopies, *e.g.* surface enhanced Raman scattering (SERS), surface enhanced fluorescence (SEF) and surface enhanced IR absorption (SEIRA) spectroscopy.[16–18] The ability of plasmons to efficiently decay through coupling to phonons can potentially enable the combination of sensing and therapy, using hyperthermia to directly damage target cells, or to trigger the *in situ* release of a cargo.[11] For example, Topete *et al.* demonstrated a nanotheranostic platform made of poly(lactic-co-glycolic acid) /doxorubicin-core@Au-branched shell nanostructures,[19] whereas Chen *et al.* reported a theranostic system obtained by co-encapsulation of iron oxide nanoparticles and gold nanorods inside mesoporous silica beads, which displayed multimodal imaging ability, combined with improvements in stroke therapy.[20] More recently, Kolovskaya *et al.* proposed high anti-cancer activity of aptamer-conjugated, spherical gold nanoparticles in tumor bearing mice upon photothermal treatment.[21] Despite these efforts, several challenges are still to be overcome before nanoplasmonics can be implemented as a tool for *in vivo* biosensing and bioimaging. The biocompatibility/toxicity of plasmonic nanoparticles has been linked to their size, shape, and surface chemistry,[22–25] and in the case of silver, to their easy oxidation leading to release of Ag^+ ions.[9,26–30] Moreover, the exposure to complex biological environments has been shown to have drastic effects on the stability and pharmacokinetics of noble metal nanoparticles.[31,32] Phenomena like protein corona formation,[33] shear forces inside the blood stream, changes in pH or temperature,[26] or immune system activity,[34,35] must be taken into account. As a matter of fact, the design of plasmonic diagnostic and theranostic nanosystems for application under *in vivo* conditions gets complicated by issues such as oxidation, unwanted ligand exchange, unspecific cellular uptake, and biodegradation.[36] These problems have led to the development of a variety of coating strategies,[37] involving polymers,[38–43] di-block and tri-block copolymers,[44–46] silica-shells,[20,47–49] and lipid or peptide based coatings.[50,51] Some of us have

recently demonstrated the encapsulation and stabilization of hydrophobic nanoparticles (quantum dots, quantum rods, iron oxide NPs) in aqueous media, using seed emulsion polymerization techniques.[52–56] Remarkably, the polymer shells obtained through this procedure were reported to provide excellent shielding in biological environments.[53,57] We demonstrate hereby the successful application of a similar process to the generalized encapsulation of plasmonic nanoparticles composed of either gold or silver, with the ability to encapsulate either single or clustered nanoparticles, by simply varying the nanoparticle(ligand)/block copolymer ratio. The possibility of precisely tuning the overall size, from a single nanoparticle up to 200 nm clusters, is of paramount importance for both *in vitro* and *in vivo* applications, as size is an essential parameter regulating nanoparticle cellular uptake.[58,59] Grzelczak *et al.* have developed a similar polymer encapsulation strategy for gold colloids based on hydrophobic interactions, but skipping the cross-linking step and with limited variation of polymer chain length.[44] Our findings show that the formation of a highly cross-linked polymer shell not only confers to the particles high stability in biological media, but also provides high resistance against extreme oxidizing conditions (*e.g.* up to 24 h in 10% *aqua regia* solution). The prepared nanostructures were incubated with different cell lines to address their biocompatibility and bio-stability, showing high cell viability ratios for all tested conditions, in combination with high cellular uptake. Electron microscopy/tomography analysis of incubated cells demonstrates the intracellular stability of the nanostructures, with a clearly visible polymer coating, even after uptake inside endosomes.[34,60]

The seeded emulsion polymerization methodology proposed here presents two important advantages over previous methods: i) interparticle distances below 3 nm within the clusters (leading to plasmon coupling and hot spot formation); ii) remarkable resistance towards high-ionic strength environment and extreme oxidizing conditions. Additionally, the proposed multi-step strategy offers wide-ranging opportunities of adaptation to specific targets and applications, ranging from the co-encapsulation of different nanoparticles and molecules,[53] through the chemical modification of the polymeric shell,[57] to the grafting of specific biomolecules to the cluster surface.[52] As such, this work represents a step forward toward the stabilization of plasmonic nanoparticles for *in vivo* applications, with potential uses as SERS bioimaging tags, photothermal therapy agents, and drug delivery systems.

Results and Discussion

The present approach is based on a seeded emulsion polymerization technique developed by Weller and co-workers,[54,61] which involves three separate steps (**Scheme 1**): (i) ligand exchange reaction with poly(isoprene)-diethylentriamine, PI-DETA; (ii) encapsulation of the hydrophobic nanoparticles in aqueous media, inside a supramolecular system formed upon addition of poly(isoprene)-*block*-poly(ethylene oxide), PI-*b*-PEO (also named PI-*b*-PEG); and (iii) seeded emulsion polymerization performed in the hydrophobic part of the system, yielding a cross-linked, protective polystyrene shell.

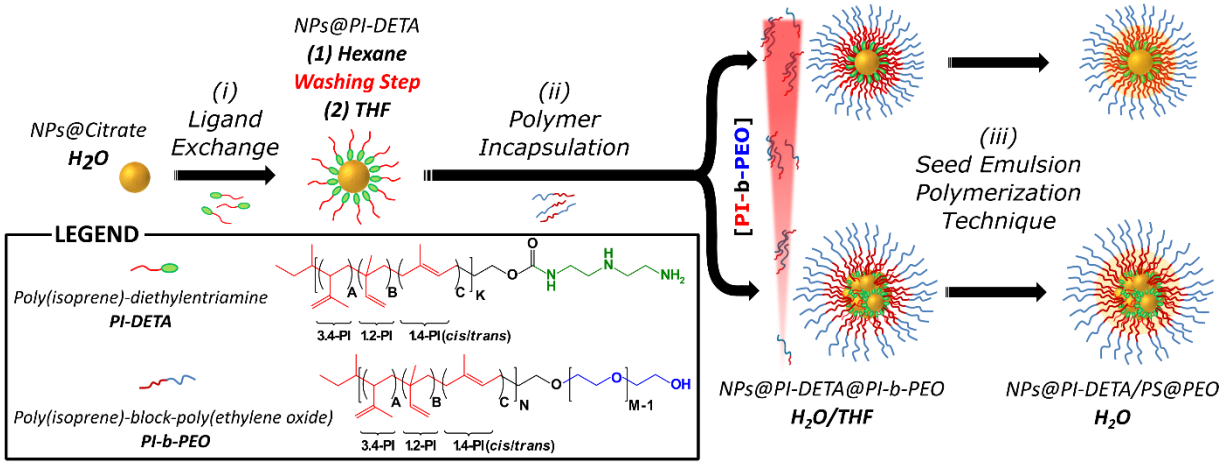

Scheme 1. Schematic representation of the three-step procedure for the encapsulation of hydrophilic nanoparticles using PI-DETA, PI-*b*-PEO di-block copolymer and seeded emulsion polymerization.

Citrate coated gold and silver nanoparticles in aqueous dispersion were selected as model plasmonic nanoparticles.[62,63] Even though both gold and silver spherical nanoparticles can be directly synthesized in organic solvents, demonstration of the encapsulation of initially hydrophilic particles provides more extensive generality to the method, *e.g.* toward the encapsulation of anisotropic nanoparticles (with plasmon resonances within the biological transparency window: 650 - 1350 nm). Although synthetic routes in organic media are limited for such particles, successful transfer from water and stabilization in non-polar solvents have been reported, and can be adapted to the protocol proposed here.[56,64,65] The ligand exchange reaction (step (i) in **Scheme 1**) was performed by emulsifying an aqueous suspension of nanoparticles together with a hexane solution of PI-DETA, through vigorous magnetic stirring (Experimental Section). The coloration of the organic phase and simultaneous discoloration of the aqueous phase, along with UV-vis

investigations, confirm successful ligand exchange and nanoparticle phase transfer (insets in **Figure 1C, E)**. The protocol was optimized by adjusting the number of PI-DETA equivalents to be added to the organic phase (see Supporting Information, **Figure S1**). We found that a minimum of 3000 PI-DETA molecules per particle are required for the effective phase transfer of 19±2 nm gold nanoparticles (**Figures S2-S4**). This corresponds to approximately 3 ligand molecules per nm^2 of gold surface, in line with the values reported in previous studies for similar polymer ligands.[66,67] It is important to note that nanoparticle phase transfer does not work in basic pH, at which amine moieties are deprotonated (Supporting Information, **Table T1**); this suggests that the charge of the anchoring group is a determining factor, probably related to the ability of the amphiphilic polymer to form micelles in water.[68] Further details on the optimization can be found in the Supporting Information (**Figures S1-S4**). The protocol was successfully adapted to 42±9 nm silver nanoparticles, using the same PI-DETA surface density as that used for gold nanoparticles (insets in **Figure 1D, F**). For both metals, UV-Vis extinction spectra before and after ligand exchange show the expected red-shift due to increased refractive index (upon ligand exchange and transfer from water to hexane), with no evidence of aggregation (**Figure 1A**). Optical data were confirmed by dynamic light scattering (DLS) analysis. For both gold and silver we observed an increase of the hydrodynamic radius by 8 nm (24 to 32 nm for gold; 60 to 68 nm for silver, see grey areas in **Figure 1B**), which confirms the exchange of citrate by the polymeric ligand PI-DETA (**Figure 1B**). TEM images confirmed that the average size distribution of the metallic colloids remained unaltered upon ligand exchange (19±3 nm to 19±2 nm; 42±9 nm to 41±8 nm, for gold and silver respectively, see **Figure 1C-F**). The presence of the PI-DETA shell cannot be appreciated through electron microscopy, as the molecular weight of the polymer, and consequently the length of the chain, are too low to offer any contrast around metal particles of this size.

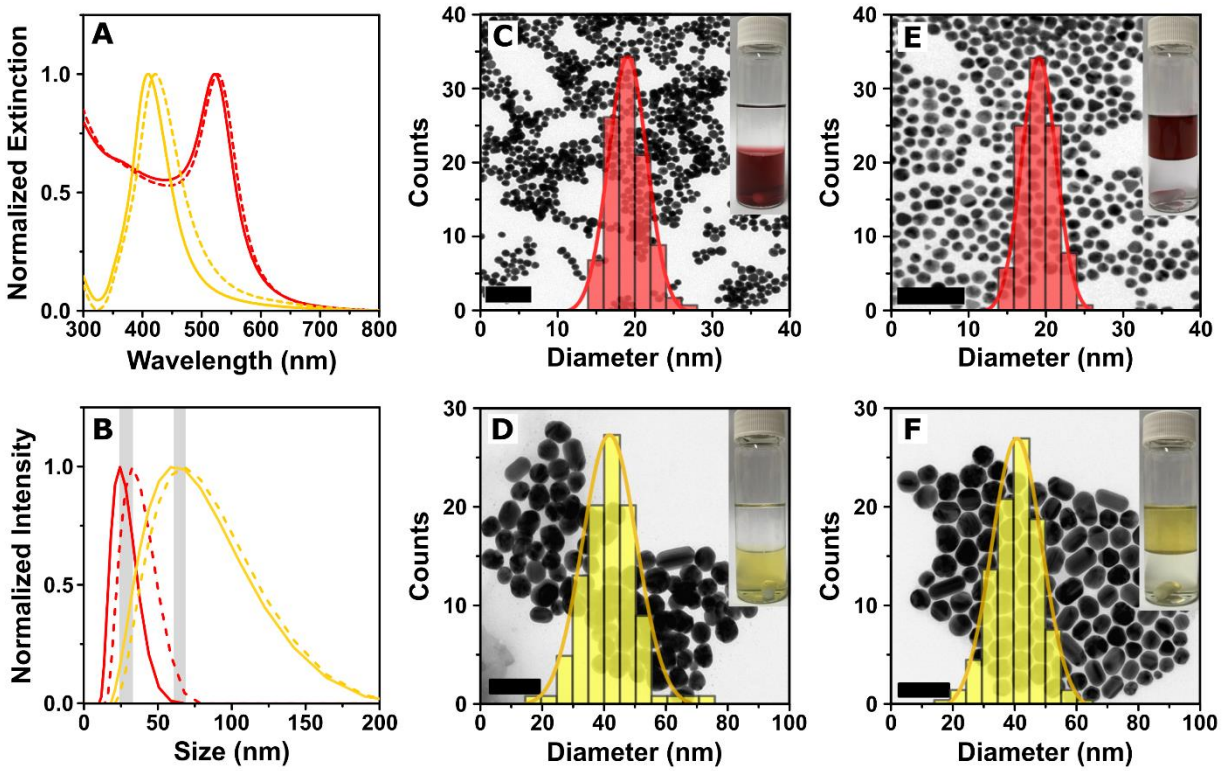

Figure 1. Normalized UV-vis spectra (**A**), and DLS analysis (**B**, intensity distribution), of citrate- (**solid lines**) and PI-DETA- (**dotted lines**) capped gold (**red lines**) and silver (**yellow lines**) nanoparticles. The grey areas in **B** highlight the difference in hydrodynamic diameter between citrate-, and PI-DETA-capped colloids. **C-F:** TEM images and size histograms for gold (**C, E**) and silver (**D, F**) nanoparticles, before (**C,D**) and after (**E,F**) ligand exchange (100 particles were counted in each case). Scale bars: 100 nm. **Insets:** photographs of the two-phase system used for ligand exchange (hexane over water).

The hydrophobic colloids obtained upon ligand exchange with PI-DETA can be dried and readily redispersed in THF, showing high stability over long periods of at least 6 months (**Figure S5**). PI-DETA coated nanoparticles were subsequently transferred back into water, using an amphiphilic PI-*b*-PEO di-block-copolymer: hydrophobic interactions between poly(isoprene) chains on the particles and in the copolymer, trigger the formation of a supramolecular micellar system (step (ii) in **Scheme 1**). This procedure can be applied, not only to the encapsulation of single nanoparticles but also to clusters of different sizes by simply changing the molar ratio between NPs@PI-DETA and PI-*b*-PEO.[56,69] The mixture of both components is readily achieved using a microfluidic system with suitable mixing chambers (see Experimental Section and **Figure S6** for details), which provide an excellent control over the shear forces generated during mixing.[69,70] This setup

prevents high concentration gradients, thereby enabling improved reproducibility in the formation of nanoparticle micelles, as compared to that obtained by manual operation. After encapsulating the particles and dispersing them in water, the final step (*iii* in **Scheme 1**) comprises an *in situ* radical polymerization reaction (see Experimental Section for detailed procedure). Briefly, THF is separated from the nanoparticle aqueous suspension by evaporation at 60 ºC for 15 min, and any remaining residues were removed under vacuum. Styrene and divinylbenzene were then immediately added to the mixture under vigorous stirring, followed by a water-soluble radical initiator to trigger the formation of a polystyrene shell within the hydrophobic part of the system, surrounding the plasmonic core. The obtained samples were then purified by simple centrifugation to remove any unreacted reagents and empty supramolecular micelles. By varying the PI-*b*-PEO:PI-DETA molar ratio, both gold or silver nanoparticle clusters could be obtained (**Figures 2** and **S7**). We expected that the addition of a lower amount of PI-*b*-PEO would lead to the formation of bigger clusters, and therefore to an increase in the hydrodynamic radius (**Figure 2C, D**). Cluster formation should also induce plasmon coupling between co-encapsulated nanoparticles, leading to a red-shift of the plasmon band (**Figure 2A, B**). Optical and structural analysis indeed confirmed the predicted trends for a supraparticle micellar system (**Figure 2**), and UV-vis, DLS and TEM data are summarized in **Table 1** and in **Figures S8, S9**. A lower energy plasmon mode becomes more relevant as the dimensions of the clusters increase, in agreement with plasmonic coupling inside the polymer shell (**Figure 2A**). In the case of the larger silver nanoparticles (~40 nm) the difference is more pronounced and additional modes can be observed for the bigger clusters (**Figure 2B**). Electron microscopy analysis revealed the presence of a polymer shell around the metallic cores (**Figure 2E, F**), as well as the increased size and number of nanoparticles per cluster.

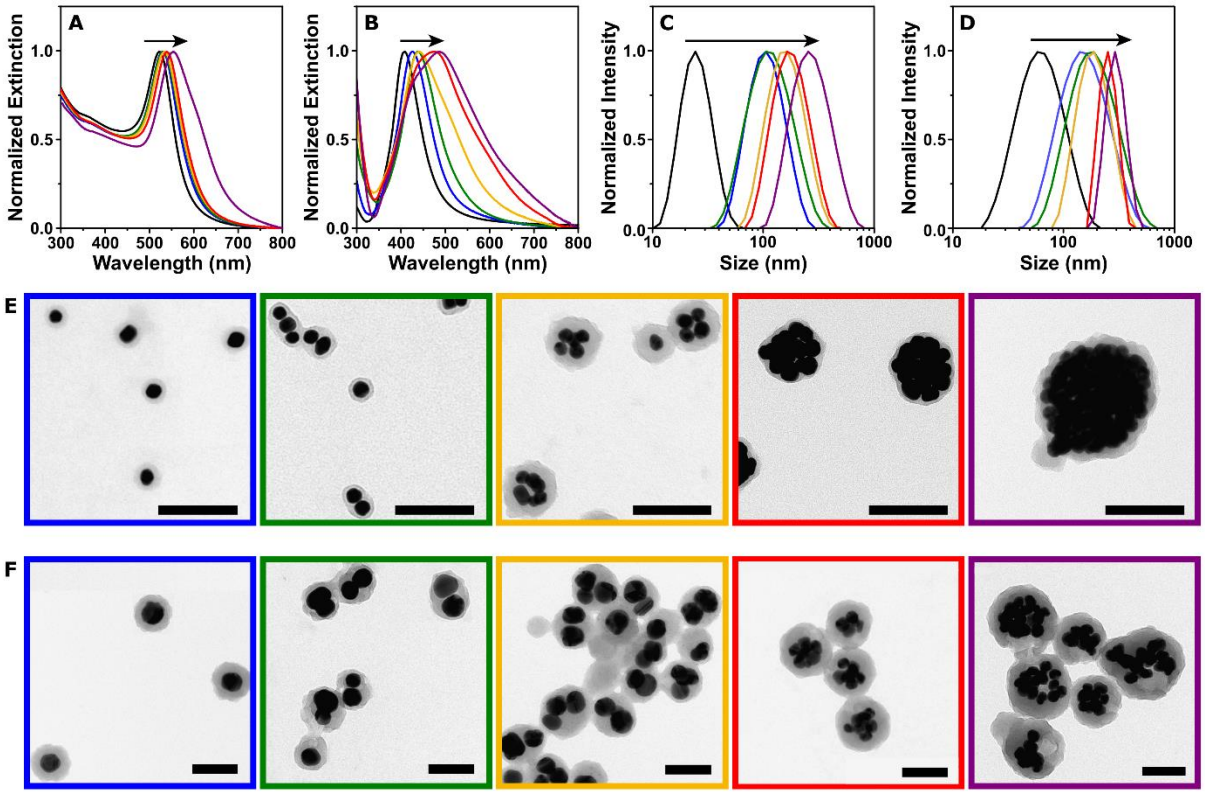

Figure 2. Normalized UV-vis spectra (**A, B**), and DLS analysis (**B, C**, intensity distribution), and representative TEM images (**E, F**) of single and clustered encapsulated gold (**A, C, E**) and silver (**B, D, F**) nanoparticles, prepared with different molar ratios between PI-*b*-PEO and PI-DETA ligands. Citrate coated nanoparticles (**black lines**, see TEM in **Figure 1**); PI-*b*-PEO:PI-DETA ratios: 1:2.5 (**blue lines**), 1:10 (**green lines**), 1:20 (**yellow lines**), 1:30 (**red lines**), 1:60 (**purple lines**). The color code is the same for all three analyses. Black arrows underline the red shift of plasmon resonances. Scale bars = 100 nm. Additional low magnification images can be found in the Supporting Information, **Figure S7**.

Gold Nanoparticles					
PI-b-PEO:PI-DETA	**1:2.5**	**1:10**	**1:20**	**1:30**	**1:60**
LSPR λ_{MAX} (nm)	528	531	534	539	552
D_H, DLS (nm)	112 ± 45	124 ± 58	168 ± 68	186 ± 73	286 ± 121
D, TEM (nm)	34 ± 3	42 ± 9	70 ± 10	70 ± 15	120 ± 20
Silver Nanoparticles					
PI-b-PEO:PI-DETA	**1:2.5**	**1:10**	**1:20**	**1:30**	**1:60**
LSPR λ_{MAX} (nm)	426	439	441	470	487
D_H, DLS (nm)	171 ± 73	203 ± 86	198 ± 42	259 ± 54	303 ± 66
D, TEM (nm)	85 ± 8	88 ± 8	100 ± 10	130 ± 20	170 ± 40

Table 1. Optical and structural data from plots presented in **Figure 2** for PI-*b*-PEO-encapsulated gold and silver nanoparticles. LSPR maxima were determined by UV-vis spectroscopy. The intensity weighted mean hydrodynamic diameter D_H were determined by DLS. Numbers of nanoparticles per micelle were determined by manual counting of 100 clusters from TEM images (see **Figures S8, S9**).

Conventional TEM measurements correspond to 2D images of 3D objects and therefore, such an analysis can be misleading for complex three-dimensional objects such as those in this study.[71] We therefore used HAADF-STEM and TEM electron tomography to visualize the clusters in three dimensions (**Figure 3**). The analysis confirmed that nanoparticle clusters feature a quasi-spherical shape (**Video 1,** Supporting Material). In order to prevent any flattening or other deformations of the polymer shell in contact with the supporting layer during sample preparation, a freeze-drying approach was applied to the TEM grid under cryo conditions, as explained in detail in the Experimental Section. This allowed us to characterize the nanoparticle packing inside the polymer shell. We found an average interparticle distance of 3±1 nm (see Experimental Section for details), which is again in agreement with the observed plasmon coupling and suggests the formation of plasmonic hot spots at the gaps between co-encapsulated particles. This represents an important advantage of our seeded emulsion polymerization approach, as compared to another polymeric encapsulation procedures, where plasmon coupling between co-encapsulated particles is limited by longer interparticle distances.[44] Moreover, by varying the length of the PI-DETA ligands used in the initial step, the interparticle distance can be tuned. Such plasmonic hot spots can be exploited for the development of bioimaging SERS-based tags.[72]

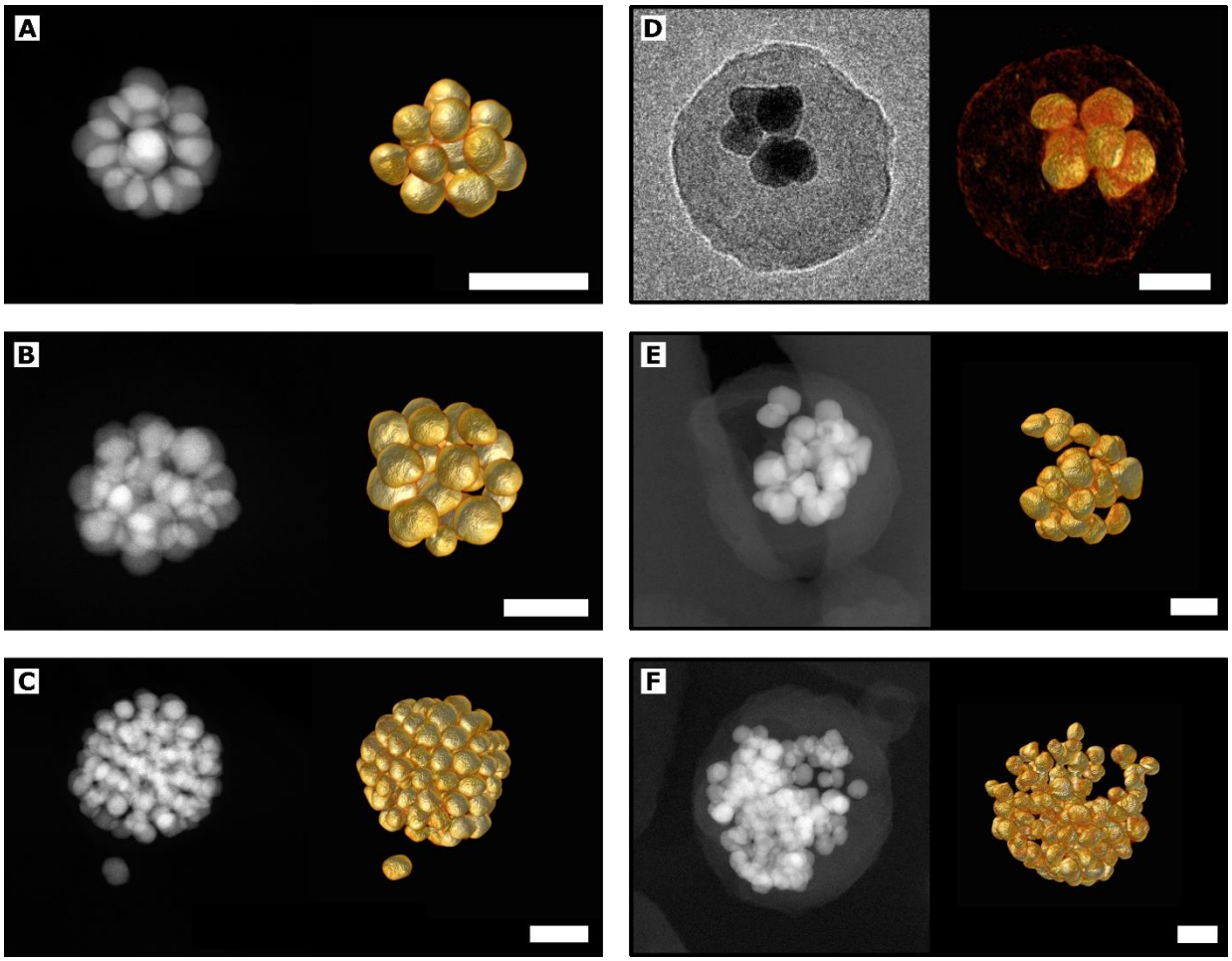

Figure 3. HAADF-STEM images (A-C, E-F left panels), TEM image (D left panel) and electron tomography reconstructions (right panels) of encapsulated clusters made of gold (**A-C**) and silver (**D-F**) nanoparticles. Using the 3D reconstructions it is possible to count the number of particles in each cluster: **A:** 14, **B:** 24, **C:** 1 | 113, **D:** 6, **E:** 31, **F:** 152. Scale bars: 50 nm.

The modular character of the encapsulation process enhances its versatility, meaning that it can be adapted to different particle sizes, shapes, and compositions, with tailored interparticle distances, as well as the possibility to encapsulate small molecules and include additional functionalities on the outer surface of the clusters. A potential drawback however, is the limited control over the number of encapsulated NPs and overall cluster size. Standard centrifugation allows eliminating larger aggregates, empty polymer micelles, as well as other organic impurities derived from polymerization (see Experimental Section and Supporting Information). Continuous density gradient centrifugation can be used to further narrow down the size distribution,[69,73] but this technique can only be applied to small volumes (up to 500 µL), and it requires extraction and

dialysis steps that render the process exceedingly long and cumbersome. Additional details and characterization for this purification procedure are provided in the Supporting Information (**Figure S10**). We postulate that the formation of a protective polystyrene shell around the metallic core of our plasmonic nanostructures should confer high biocompatibility, protection against oxidizing environments, stability under physiological conditions, and high cellular uptake. We thus investigated the stability of both encapsulated single nanospheres and clusters, made of Au and Ag, before and after seeded emulsion polymerization, under strongly oxidizing conditions. This analysis is of particular relevance in the case of Ag nanoparticles, since the oxidation of metallic silver is considered to be the main reason behind their intrinsic cytotoxicity.[9,27,30] We tested the oxidation of Au nanostructures by nitric acid (0.1% v/v), aqua regia (0.1% v/v), and potassium cyanide (34 equivalents), whereas silver particles were incubated in solutions of nitric acid (0.1% v/v), aqua regia (0.1% v/v), and hydrogen peroxide (0.1% v/v). Even though nitric acid cannot dissolve metallic gold, the high ionic strength might still induce nanoparticle precipitation, as observed for citrate-capped colloids. **Figure 4** summarizes our results, which confirm a remarkably different behavior for encapsulated nanoparticles, as compared to citrate-stabilized colloids. As can be clearly appreciated from UV-vis spectra, all coated samples were stable over 24 hours, whereas citrate-nanoparticle colloids were rapidly oxidized (**Figures S11, S12**). Encouraged by these results, we also tested stability of nanoparticle clusters under extreme oxidizing conditions, by incubation in a 10% *aqua regia* solution. Remarkably, the protective polymer shell was still able to provide stability to the clusters for over 24h, in contrast to unprotected samples, which were completely oxidized within a few seconds (**Figure S13**). This high resistance towards chemical oxidation represents another important advantage of our encapsulation strategy, making these hybrid plasmonic nanostructures strong candidates as long-lasting tags for *in vivo* applications.

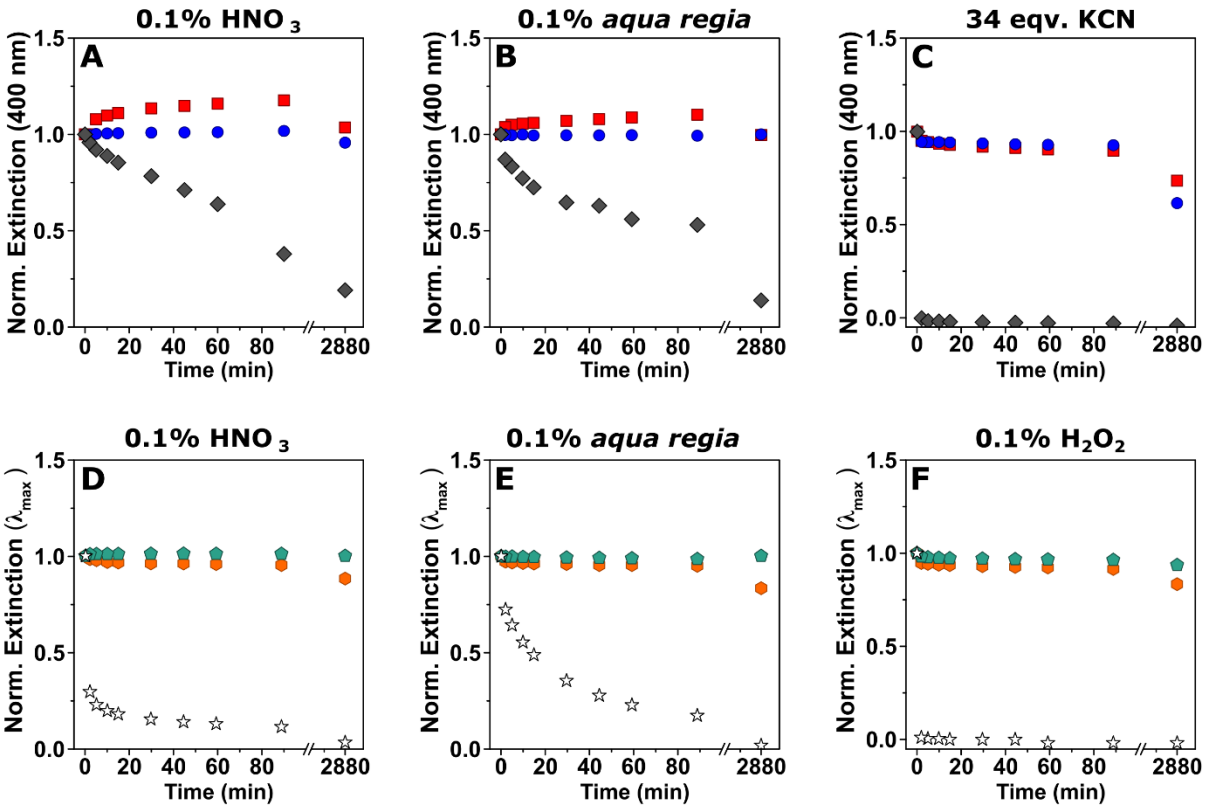

Figure 4. A-C: UV-vis spectroscopy analysis (time traces of the absorbance at 400 nm) of the stability of citrate stabilized (grey diamonds), encapsulated single gold nanoparticles (red squares, 1:2.5 PI-*b*-PEO:PI-DETA ratio) and encapsulated gold nanoparticle clusters (blue circles, 1:20 PI-*b*-PEO:PI-DETA ratio), upon incubation with 0.1% HNO_3 (**A**), 0.1% aqua regia (**B**) and KCN solution (34:1, n(KCN):n(Au^0)) (**C**). **D-F:** UV-vis spectroscopy analysis (absorbance at the maximum *vs.* time[74]) of the stability of citrate capped (white stars), encapsulated single silver nanoparticles (orange hexagons, 1:2.5 PI-*b*-PEO:PI-DETA ratio) and encapsulated silver nanoparticle clusters (green circles, 1:20 PI-*b*-PEO:PI-DETA ratio) upon incubation with 0.1% HNO_3 (**D**), 0.1% aqua regia (**E**) and 0.1% H_2O_2 (**F**). The corresponding UV-vis spectra are provided in the Supporting Information (**Figures S11, S12**).

Finally, the *in vitro* stability and biocompatibility of the synthetized hybrid plasmonic nanostructures were investigated by TEM of fixed and resin embedded mammalian cell samples, as well as by MTT cell viability assays. Three different cell lines were tested: HeLa and A549 as cancerous cell lines, and human dermal fibroblasts (HDF) as healthy primary cells. We observed that exposure of HeLa and A549 cells to concentrations of Au or Ag nanoparticles above 3 µM resulted in a decrease of their metabolic activity compared to control cells (**Figure 5A, B** and **Figures S14, S16**). Although decreased MTT assay readouts are generally interpreted as a sign of

reduced cell viability, optical microscopy observations dismissed any nanoparticle-induced cytotoxicity at these concentrations (**Figure 5C-F** and **Figure S15**). We thus propose that the high levels of nanoparticle uptake may have an inhibitory effect on the metabolic activity of these highly proliferative cells, as compared to control samples (**Figure S15**). Indeed, various examples of chemical compounds or nanoparticles causing over/underestimation of cell viability when using the MTT assay can be found in the literature.[75,76] The MTT assay measures the reduction of tetrazolium dye MTT by mitochondrial enzymes, thereby giving information on the cellular metabolic activity, but is not a direct measure of toxicity.[77] Interestingly, MTT results from less metabolically active HDF cells, show levels of cell viability nearly equal to control cells at concentrations up to 30 µM for both Au and Ag, even though the nanoparticle uptake is obviously very high (**Figure S16**), which further supports our hypothesis.

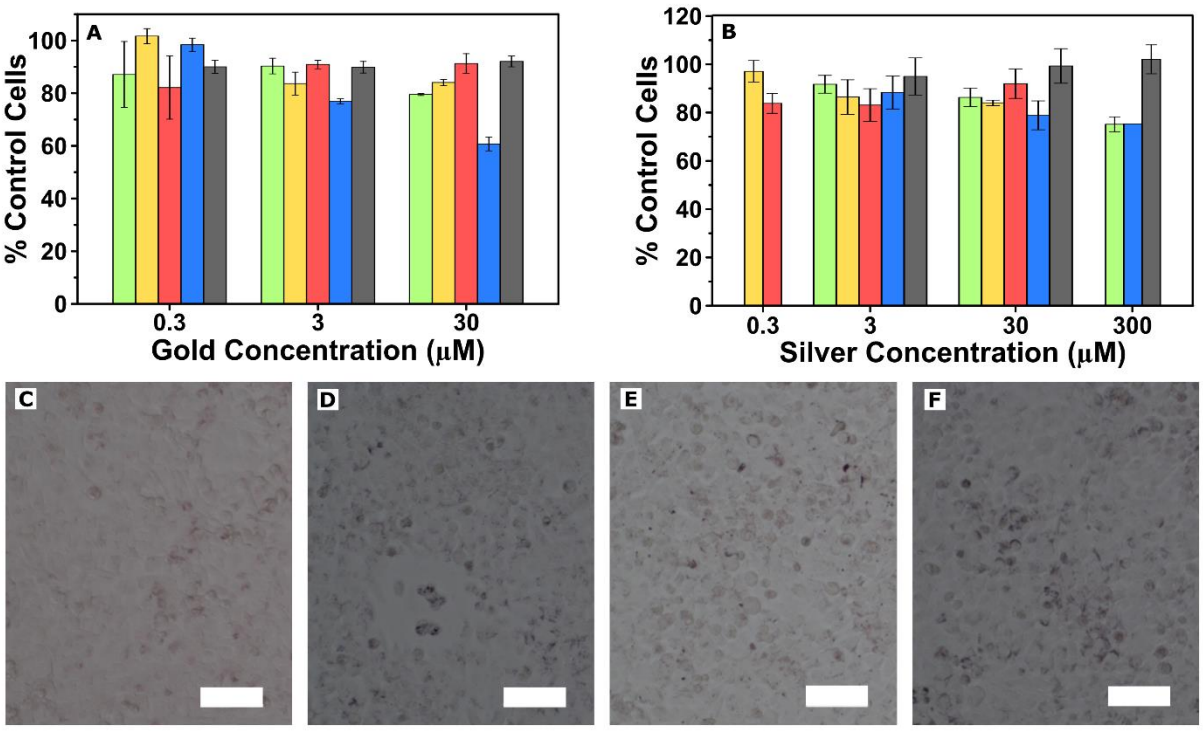

Figure 5. **A, B:** Metabolic activity of HeLa cells incubated with clusters of different sizes, expressed as % of control cells, measured with the MTT assay after exposure to different concentrations of Au (**A**) and Ag (**B**) nanoparticles. PI-*b*-PEO:PI-DETA ratios: 1:2.5 (**green**), 1:10 (**yellow**), 1:20 (**red**), 1:30 (**blue**), citrate colloids (**grey**). **C-F:** Light microscopy images of HeLa cells incubated with 30 µM encapsulated gold clusters. PI-*b*-PEO:PI-DETA ratio: 1:2.5 (**C**), 1:10 (**D**), 1:20 (**E**), 1:30 (**F**). Scale bars: 100 µm.

We observed that all nanoparticle formulations were endocytosed in high amounts for all three cell lines. *In vitro* nanoparticle stability was additionally assessed *via* TEM analysis of HeLa cells exposed to the various gold and silver nanostructure formulations, confirming intracellular stability in all cases (**Figure 6** for gold and **Figure S17** for silver). Even inside endosomal vesicles where the pH is commonly more acidic (pH~ 4.5-5.5) the polymeric shells around the clusters can be observed with no apparent degradation (**Figure 6G-I** and **Figure S17**). The presence of the polymer shell is even more evident when compared to internalized gold and silver nanoparticles that are simply coated with citrate (**Figure S18**). Moreover, citrate coated silver nanoparticles show clear signs of degradation after internalization (**Figure S18**).[30,78]

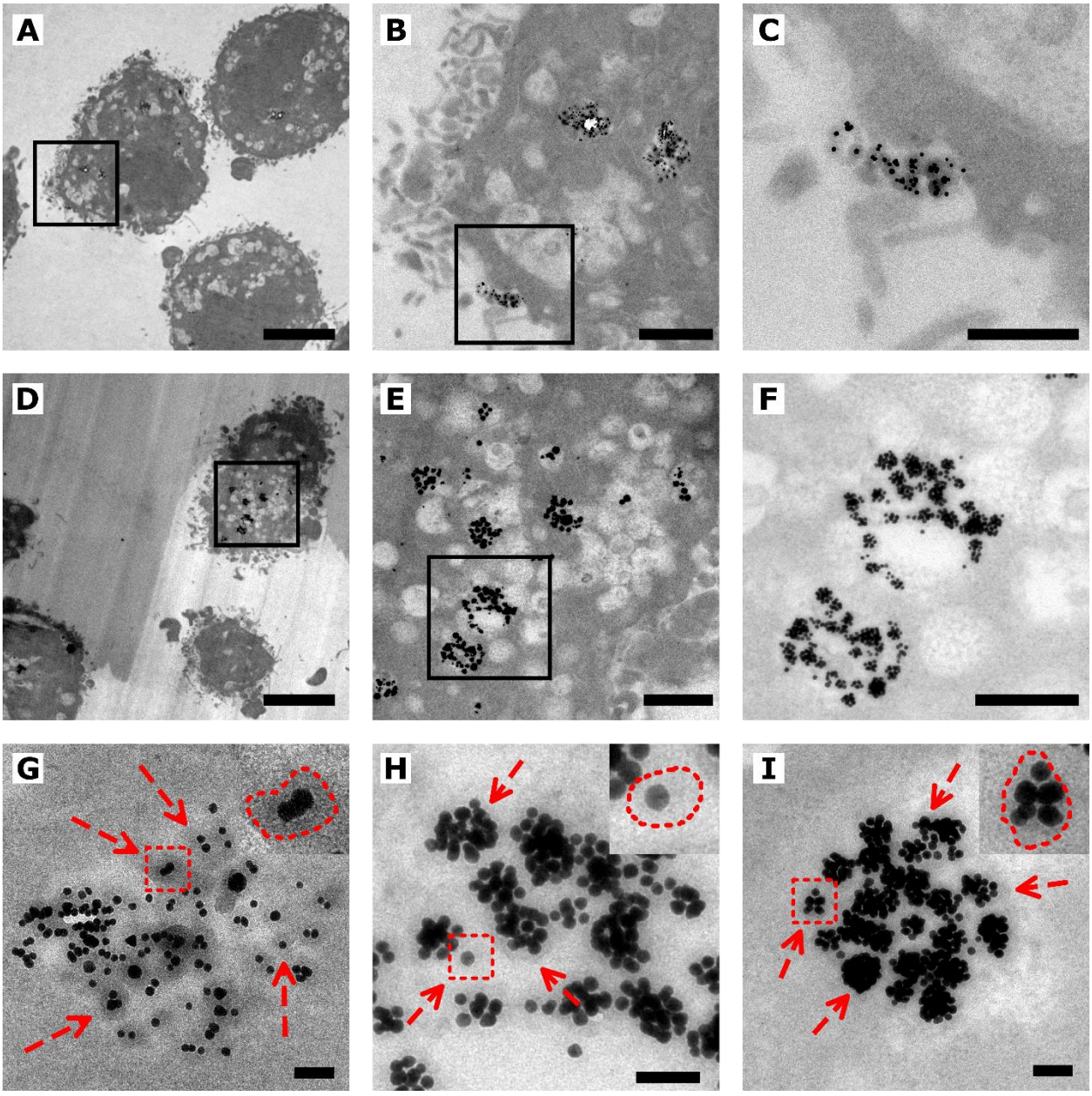

Figure 6. A-F: Representative TEM images at different magnifications showing the cellular uptake by HeLa cells, of gold clusters with PI-*b*-PEO:PI-DETA ratios of 1:10 (**A-C**), and 1:20 (**D-F**). **G-I**: High magnification images of uptaken clusters, where the polymeric shell can be distinguished (red arrows), confirming the stability of clusters after internalization inside endosomal vesicles. **Insets**: higher magnification images of the dashed red square box areas. The red dashed lines in the insets serve as a guide for the eye, marking the polymeric shells. Scale bars: **A, D**: 5 µm; **B, E**: 1 µm; **C, F**: 500 nm; **G-I**: 100 nm.

Conclusions

A three-step seed emulsion polymerization process was implemented for the encapsulation of plasmonic nanoparticles. This procedure does not impose any limitations on particle size, shape or composition. We focused here on the encapsulation of gold (19±2 nm) and silver (42±9 nm) nanoparticles. By varying the di-block-copolymer/nanoparticles ratio, the overall size of nanoparticle clusters could be tuned up to 200 nm, by increasing the number of co-encapsulated building blocks. Optical analysis revealed the presence of plasmon coupling between nearby nanoparticles within the clusters, which can potentially be exploited for the enhancement of weak optical signals at hot spots. Most importantly, the polymer shell around the nanoparticles proved to be an effective barrier against both aggregation and oxidation, under high ionic strength and extreme oxidizing conditions, respectively: both gold and silver nanoparticles remained unchanged for over 24 hours, even when immersed in a 10% *aqua regia* solution. We demonstrated biocompatibility of encapsulated single particles and clusters, by incubation of Au and Ag nanoparticles with three different cell lines, which showed high cell viability despite of very high cellular uptake. Electron microscopy analysis of incubated cells demonstrated the intracellular stability of the nanostructures, with a stable polymer coating, even after uptake into endosomes.
Overall, the proposed strategy represents a significant step forward toward the stabilization of plasmonic nanoparticles for *in vivo* applications. It is worth noting that the modular nature of our protocol offers the possibility to fine-tune the physicochemical properties of the hybrid systems, which will be the subject of upcoming research, aiming at the development of diagnostic and theranostic nanosystems.

Acknowledgements

This work was supported by the Spanish MINECO (Grant MAT2017-86659-R), by the German Research Foundation (DFG) via grant LA 2901/1-1 and by the European Research Council 289 (Grant 335078 COLOURATOM to S.B). The authors acknowledge funding from the European Commission Grant (EUSMI 731019 to 292 S.B., L.M.L.-M). L.S. acknowledges funding from the American-Italian Cancer Foundation through a Post-Doctoral Research Fellowship. D.J.d.A. thanks MINECO for a Juan de la Cierva fellowship (IJCI-2015-24264). J.P.M. was financed by

Verband der Chemischen Industrie e.V. (VCI). We thank Dr. Artur Feld, Dr. Andreas Kornowski and Stefan Werner (Institute of Physical Chemistry, University of Hamburg) for their support.

Keywords

encapsulation, gold nanoparticles, polymer micelles, self-assembly, silver nanoparticles

ASSOCIATED CONTENT

Supporting Information Available: Additional TEM images, tomographic reconstruction and UV-vis-NIR spectra, analysis of NPs dimensions, discussion on nanoparticle phase transfer, purification by continuous density gradient centrifugation, stability tests, and cellular uptake experiments. This information is available free of charge via the Internet at http://pubs.acs.org/.

EXPERIMENTAL SECTION

Instrumentration. Ultraviolet-visible (UV-vis) spectroscopy was performed on a Cary 50 (Varian) spectrometer. Dynamic light scattering (DLS) measurements were carried out on a Malvern Zetasizer Nano ZS system with a single angle 173° backscattering system, using He-Ne laser illumination at 633 nm. Transmission electron microscopy (TEM) images were recorded with a JEOL JEM-1011 microscope (100 keV). High angle annular dark field scanning TEM (HAADF-STEM) and conventional TEM images were acquired using a FEI Tecnai and a FEI Osiris electron microscopes operated at 200 kV. The acquisition of electron tomography image series was performed in HAADF-STEM and TEM mode by using a Fischione model 2020 single tilt tomography holder. The series were acquired in the tilt range from -72^{o} to +72^{o}, with tilt increment of 2^{o}. The reconstruction of tilt series was performed using the Astra Toolbox for MATLAB. The visualization of the 3D reconstructions was performed using Amira software.

Freeze-drying procedure. Plunge freezing of the grid was performed with the FEI Vitrobot instrument as follows: the TEM grid is loaded inside the equipment and a drop cast of the solution

is deposited on the grid. The excess of liquid is blotted with a filter paper and the grid is immediately immersed in liquid ethane (temperatures ≤ 180 ºC). The grid was transferred to the Fischione model 2550 cryo-transfer tomography holder in the presence of liquid nitrogen (temperatures ≤ 160 ºC). Next, heating of the grid is performed inside a vacuum chamber, with pressure below $5x10^{-6}$ mbar and with temperature rate of +2.6 ºC, until room temperature. These conditions enabled the phase transition of the vitreous ice layer from solid state to gaseous state without going through liquid state, minimizing the artefacts related with the drying process.[79]

Determination of interparticle distance. TEM tomography series were acquired of the cluster prepared after the freeze-drying procedure. In this manner, the delivered dose is smaller when compared with the conventional HAADF-STEM. The definition of interparticle distance corresponds to the distance between the edges of a pair of nanoparticles. This distance was determined through the slices of the three-dimensional reconstruction and the smallest distance here corresponds to the interparticle distance.

Materials. Trisodium citrate (Fluka), ascorbic acid (Sigma Aldrich), hydrogen tetrachloroaurate (Alfa Aesar), silver nitrate (Merck) and 2,2'-azobis[2-(2-imidazolin-2-yl)propane]dihydrochloride (VA-044, Wako Chemicals) were used as received from commercial sources. Poly(isoprene)-diethylenetriamine (PI-DETA) and poly(isoprene)-*block*-poly(ethylene oxide) (PI-*b*-PEO) were provided by CAN GmbH (Center of Applied Nanotechnology, Hamburg, Germany) and prepared via living anionic polymerization according to Pöselt *et al*.[52] The average molecular weight of PI-DETA (M_w ~ 1300 g·mol^{-1}) and PI-*b*-PEO (M_w ~ 13400 g·mol^{-1}; M_n ~ 12600 g·mol^{-1}, 65 wt% PEO) were determined from size-exclusion chromatography analysis. Styrene (analytical grade, Merck) and divinylbenzene (technical grade, ~ 55% para-isomer), Merck) were purified by distillation. Water was purified using a Purelab Flex 2 system (18.2 MΩ cm) and flushed with nitrogen for at least 6 h before each use. Anhydrous, butylated hydroxytoluene (BHT, 0.025 – 0.04%) stabilized Tetrahydrofuran (THF, VWR Chemicals) was used to prevent peroxide formation and contamination. The other solvents were of analytical grade.

Synthesis of Gold Nanoparticles. A 600 mL colloid containing ~20 nm diameter citrate-stabilized gold nanoparticles was prepared as previously reported.[62] The concentration of colloidal gold was determined from the UV-Vis absorbance at 400 nm.[80]

Synthesis of Silver Nanoparticles. Citrate-stabilized ~40 nm diameter silver nanoparticles (250 mL) were synthesized following ref. [81]. The concentration of colloidal silver was determined by UV-Vis spectroscopy. [74]

Ligand Exchange. Nanoparticles were transferred from water into *n*-hexane (VWR Chemicals) upon ligand exchange of citrate by hydrophobic PI-DETA. Then, 12.5 mL of a citrate-stabilized nanoparticle dispersion was mixed with 7.5 mL of a PI-DETA/*n*-hexane solution in a 40 mL vial. The PI-DETA concentration (c(PI-DETA), **Table 2**) was adjusted based on the total particle surface area, assuming perfectly spherical objects. Phase transfer was performed by emulsifying the two phases through vigorous magnetic stirring in a closed vial for at least 15 min. Discoloration of the aqueous phase and coloration of the organic phase confirmed ligand exchange and phase transfer (**Figure 1**). The progress of phase transfer was verified by UV-Vis spectroscopy. On completion, the organic phase was separated by means of a 25 mL separating funnel. The nanoparticles were stored at 4 °C in the dark.

Microfluidics Encapsulation. The nanoparticle dispersion in *n*-hexane was centrifuged (9,000 - 13,000 g, 15 min, 10 °C). The supernatant was removed, the black precipitate dried thoroughly under nitrogen flow and the nanoparticles resuspended in 1 mL THF. The suspension was centrifuged again and concentrated to 300 µL. Subsequently, 500 µL THF and a THF/PI-*b*-PEO stock solution (75 µM, V(PI-*b*-PEO), **Table 2**) were added. The PI-*b*-PEO concentration was adjusted based on the molar ratios of PI-*b*-PEO relative to the added amount of the PI-DETA; this ratio will be expressed as PI-*b*-PEO:PI-DETA throughout the manuscript (1:2.5 – 1:60). Nanoparticle encapsulation was realized using a computer-controlled flow system (neMESYS pump from Cetoni, Gera, Germany) equipped with a microfluidic reactor chip consisting of 45 µm diameter microfluidic mixing chambers.[82] The THF/nanoparticles@PI-DETA/PI-*b*-PEO solution was mixed with water using the flow system schematized in **Figure S6**, with a final volume ratio of 1:9. The resulting solution was incubated for 15 min at room temperature on an orbital shaker at 150 rpm.

Seeded Emulsion Polymerization. Emulsion polymerization was carried out under nitrogen-atmosphere and all glass devices and stir bars were cleaned with *aqua regia* and rinsed with DI water before use. The suspension of PI-*b*-PEO encapsulated nanoparticles was diluted with water to 25 mL in a 50 mL three-neck round-bottom flask. The solution was then stirred for 15-30 min at 60 °C to remove the THF. Afterwards, the flask was closed, gently evacuated and again flushed with nitrogen. Subsequently, styrene and divinylbenzene (*V*(Styrene) and *V*(DVB), **Table 2**) were added and incubated for 15 min in a closed flask under stirring at 60 °C. The amount of monomer can be varied depending on the desired shell thickness, if the molar ratio *p*-DVB:Styrene is kept constant at 1:10. To start the polymerization, 100 µL of a freshly prepared aqueous solution of the radical initiator 2,2'-Azobis[2-(2-imidazolin-2-yl)propane]dihydrochloride (VA-044, Wako Chemicals, *c*(VA-044), **Table 2**) was added. The solution was stirred for 3 h at 60 °C in a closed flask. Empty micelles were removed via centrifuging (500 - 3000 g, 15 min) and discarding the supernatant.

Table 2. Conditions for standard ligand exchange and seeded emulsion polymerization. *c*(NPs@Citrate) is the concentration of nanoparticles in the initial aqueous colloidal dispersion, *d* is the average particle diameter (from TEM analysis); PI-*b*-PEO stock solution is 75 µM, *V*(DVB) is based on supplier's indication on para-isomer content.

	c(NPs@Citrate) [nM]	*d* [nm]	*c*(PI-DETA) [µM]	*V*(PI-*b*-PEO) [µL]	*V*(Styrene) [µL]	*V*(DVB) [µL]	*c*(VA-044) [mM]
Gold	3.7	19.1	15.2	25 - 607	6.0	1.4	60
Silver	0.2	41.7	4.1	7 - 166	2.3	0.5	30

Continuous Density Gradient Centrifugation (CDGC). CDGC was performed according to the protocol of Steinigeweg *et al.* to obtain well defined cluster sizes.[73] The synthesized colloidal clusters were concentrated to 500 µL and stacked on top of the density gradient. The colloids were centrifuged for 60 minutes at 10 °C and 4300 g (11180 Swig Out Rotor; Sigma-3-18K). The different fractions were extracted with a horizontal curved hypodermic needle starting from the top, and purified using dialysis (Molecular weight cut-off (MWCO 3.5-5 kD)) for four days, with the wash solution refreshed three times.

Stability Tests. Stability studies were performed in quartz cuvettes with a 1 mL suspension. Absorbance was recorded by UV-Vis spectroscopy over a period of 48 h. Nitric acid (0.1 vol.%), and fresh Aqua Regia (0.1 and 10 vol.%), were tested for both gold and silver nanoparticles on the original aqueous suspensions, and on the single and clustered encapsulated nanoparticles suspensions. Additionally, KCN (0.2 M) was also tested for gold, and H_2O_2 (0.1 vol.%) was tested for silver.

Cell viability studies. The nanoparticle samples were centrifuged (1000 rpm (1:60 clusters), 1500 (1:30), 2000rpm (1:20), 2500rpm (1:10), and 3000rpm (1:2.5), for 20min, 3 times) and resuspended in water to remove large aggregates, empty polymer micelles and other impurities. Cells (HeLa, A549 or human dermal fibroblast (HDF)) were grown in DMEM media supplemented with 10% FBS and 1% PS. Cells were plated at either 1×10^4 cells/well (HeLa and A549) or 5×10^3 cells/well (HDF) in 96-well plates and allowed to adhere overnight. The following day cell media was replaced with 100 µL of gold and silver nanoparticles diluted in complete DMEM media; 10-fold dilutions starting from a maximum of 300 or 30 µM Au or Ag (in cell media) were used, depending on the original nanoparticle stock concentration. The initial dilution used was never below 1/3, thereby minimizing the cytotoxic effects of the solvent (water). Samples were incubated with cells for 48 h, followed by removal of the nanoparticles and application of the MTT assay (Roche), measuring the absorbance at 550 nm. Results are expressed as a percentage of the control cell MTT absorbance value, a measure of the metabolic activity of the cells. In the case of the highest gold nanoparticle concentration (30 µM), photos of the wells were taken using a Zeiss Cell Observer microscope equipped with a 20× objective (0.8 N.A) and color camera. All settings relating to photo acquisition and post processing (exposure time, gamma settings, etc.) were identical.

Cell Preparation for TEM. The cellular uptake and the stability of the polymeric shell inside the cell were confirmed using TEM. HeLa, A549 and HDF cells were plated in 12-well plates at 2×10^5 (HeLa, A549) or 1×10^5 (HDF) cells/well. The following day media was replaced with 800 µL nanoparticles diluted in cell media to a final concentration of 30 µM. After 48 h incubation, nanoparticles were removed and adhered cells washed with warm media. Cells were detached using trypsin and washed numerous times with Sorensen's buffer before being fixed in a solution of formaldehyde and glutaraldehyde. Samples were embedded in agarose, dehydrated in an ethanol

series, and resin embedded. 80-100 nm slides were cut on an ultramicrotome and post stained with uranyl acetate and lead citrate. TEM images were collected with a JEOL JEM- 1400PLUS transmission electron microscope operating at 120 kV, using carbon coated 400 square mesh copper grids.

Cell preparation for reflectance and fluorescence microscopy: HeLa cells were seeded in optical microscopy 96-well plates ($2x10^4$ cells/well) and allowed to adhere overnight. Cell media was replaced with 200ul cell media containing nanoparticles at a final concentration of 30 µM. After 48 h incubation, samples were imaged without washing in confocal reflectance mode (Zeiss 880 Confocal Scanning Microscope), employing a C-Apochromat 40x objective with 633 nm laser source and 18 nm detector window between 624 and 642 nm. All images used the same pinhole, laser power, photo acquisition and post-processing parameters. A 3-pixel median filter was applied to the reflectance channel and images are shown in original black-white and false coloured combined with brightfield transmission images. Following reflectance image acquisition, cell media was replaced with Live/dead staining fluorophores (Abcam; Apoptosis/Necrosis detection kit) and images acquired using excitation wavelengths of 405 nm (live fluorophore; blue), 488 nm (apoptosis fluorophore, green), and 597 nm (necrosis fluorophore, red). Again, all images used the same pinhole, laser power, photo acquisition and post-processing parameters, including a 3-pixel median filter as post-processing.

References:

[1] S. Laing, L. E. Jamieson, K. Faulds, D. Graham, *Nat. Rev. Chem.* **2017**, *1*, 0060.
[2] K. T. Nguyen, J. U. Menon, P. V. Jadeja, P. P. Tambe, K. Vu, B. Yuan, *Thernostics* **2013**, *3*, 152–166.
[3] X. Huang, I. H. El-Sayed, M. A. El-Sayed, *Methods Mol. Biol. Clifton NJ* **2010**, *624*, 343–357.
[4] L. Scarabelli, *Pure Appl. Chem.* **2018**, *90*, 1393–1407.
[5] J. A. Webb, R. Bardhan, *Nanoscale* **2014**, *6*, 2502–2530.
[6] D. J. de Aberasturi, A. B. Serrano-Montes, L. M. Liz-Marzán, *Adv. Opt. Mater.* **2015**, *3*, 602–617.
[7] M. Salim, H. Minamikawa, A. Sugimura, R. Hashim, *Med Chem Commun* **2014**, *5*, 1602–1618.
[8] M.-F. Tsai, S.-H. G. Chang, F.-Y. Cheng, V. Shanmugam, Y.-S. Cheng, C.-H. Su, C.-S. Yeh, *ACS Nano* **2013**, *7*, 5330–5342.
[9] A. Taglietti, Y. A. Diaz Fernandez, E. Amato, L. Cucca, G. Dacarro, P. Grisoli, V. Necchi, P. Pallavicini, L. Pasotti, M. Patrini, *Langmuir* **2012**, *28*, 8140–8148.
[10] P. Pallavicini, A. Dona, A. Taglietti, P. Minzioni, M. Patrini, G. Dacarro, G. Chirico, L. Sironi, N. Bloise, L. Visai, *Chem. Commun.* **2014**, *50*, 1969–1971.
[11] S. S. Kelkar, T. M. Reineke, *Bioconjug. Chem.* **2011**, *22*, 1879–1903.
[12] J. Xie, S. Lee, X. Chen, *Adv. Drug Deliv. Rev.* **2010**, *62*, 1064–1079.

[13] A. McLintock, C. A. Cunha-Matos, M. Zagnoni, O. R. Millington, A. W. Wark, *ACS Nano* **2014**, *8*, 8600–8609.
[14] H. Im, H. Shao, R. Weissleder, C. M. Castro, H. Lee, *Expert Rev. Mol. Diagn.* **2015**, *15*, 725–733.
[15] P. Yang, J. Zheng, Y. Xu, Q. Zhang, L. Jiang, *Adv. Mater.* **2016**, *28*, 10508–10517.
[16] S. Lal, N. K. Grady, J. Kundu, C. S. Levin, J. B. Lassiter, N. J. Halas, *Chem. Soc. Rev.* **2008**, *37*, 898–911.
[17] M. Moskovits, *Rev. Mod. Phys.* **1985**, *57*, 783–826.
[18] J. Wessel, *JOSA B* **1985**, *2*, 1538–1541.
[19] A. Topete, M. Alatorre-Meda, P. Iglesias, E. M. Villar-Alvarez, S. Barbosa, J. A. Costoya, P. Taboada, V. Mosquera, *ACS Nano* **2014**, *8*, 2725–2738.
[20] P.-J. Chen, Y.-D. Kang, C.-H. Lin, S.-Y. Chen, C.-H. Hsieh, Y.-Y. Chen, C.-W. Chiang, W. Lee, C.-Y. Hsu, L.-D. Liao, et al., *Adv. Mater.* **2015**, *27*, 6488–6495.
[21] O. S. Kolovskaya, T. N. Zamay, I. V. Belyanina, E. Karlova, I. Garanzha, A. S. Aleksandrovsky, A. Kirichenko, A. V. Dubynina, A. E. Sokolov, G. S. Zamay, et al., *Mol. Ther. - Nucleic Acids* **2017**, *9*, 12–21.
[22] A. M. Alkilany, C. J. Murphy, *J. Nanoparticle Res.* **2010**, *12*, 2313–2333.
[23] N. Khlebtsov, L. Dykman, *Chem. Soc. Rev.* **2011**, *40*, 1647–1671.
[24] E. S. Melby, C. Allen, I. U. Foreman-Ortiz, E. R. Caudill, T. R. Kuech, A. M. Vartanian, X. Zhang, C. J. Murphy, R. Hernandez, J. A. Pedersen, *Langmuir* **2018**, *34*, 10793–10805.
[25] L. L. Olenick, J. M. Troiano, A. Vartanian, E. S. Melby, A. C. Mensch, L. Zhang, J. Hong, O. Mesele, T. Qiu, J. Bozich, et al., *Chem* **2018**, *4*, 2709–2723.
[26] K. Park, G. Tuttle, F. Sinche, S. L. Harper, *Arch. Pharm. Res.* **2013**, *36*, 125–133.
[27] A. Ivask, A. ElBadawy, C. Kaweeteerawat, D. Boren, H. Fischer, Z. Ji, C. H. Chang, R. Liu, T. Tolaymat, D. Telesca, et al., *ACS Nano* **2013**, *8*, 374–386.
[28] L. Wang, T. Zhang, P. Li, W. Huang, J. Tang, P. Wang, J. Liu, Q. Yuan, R. Bai, B. Li, et al., *ACS Nano* **2015**, *9*, 6532–6547.
[29] B. B. Manshian, C. Pfeiffer, B. Pelaz, T. Heimerl, M. Gallego, M. Möller, P. Del Pino, U. Himmelreich, W. J. Parak, S. J. Soenen, *ACS Nano* **2015**, *9*, 10431–10444.
[30] E. Caballero-Díaz, C. Pfeiffer, L. Kastl, P. Rivera-Gil, B. Simonet, M. Valcárcel, J. Jiménez-Lamana, F. Laborda, W. J. Parak, *Part. Part. Syst. Charact.* **2013**, *30*, 1079–1085.
[31] R. A. Trbojevich, A. M. Torres, in *Met. Nanoparticles Pharma*, Springer, Cham, **2017**, pp. 451–468.
[32] T. K. Sau, A. Biswas, P. Ray, in *Met. Nanoparticles Nanomedicine Advant. Scope*, Wiley, **2018**, pp. 121–168.
[33] P. Del Pino, B. Pelaz, Q. Zhang, P. Maffre, G. U. Nienhaus, W. J. Parak, *Mater. Horiz.* **2014**, *1*, 301–313.
[34] N. Oh, J.-H. Park, *Int. J. Nanomedicine* **2014**, *9*, 51–63.
[35] L. Dykman, N. Khlebtsov, *Chem. Soc. Rev.* **2012**, *41*, 2256–2282.
[36] P. Rivera-Gil, D. Jimenez De Aberasturi, V. Wulf, B. Pelaz, P. Del Pino, Y. Zhao, J. M. De La Fuente, I. Ruiz De Larramendi, T. Rojo, X.-J. Liang, et al., *Acc. Chem. Res.* **2012**, *46*, 743–749.
[37] S. K. Nune, P. Gunda, P. K. Thallapally, Y.-Y. Lin, M. L. Forrest, C. J. Berkland, *Expert Opin. Drug Deliv.* **2009**, *6*, 1175–1194.
[38] R. Jin, *Angew. Chem. Int. Ed.* **2008**, *47*, 6750–6753.
[39] X. Qian, X.-H. Peng, D. O. Ansari, Q. Yin-Goen, G. Z. Chen, D. M. Shin, L. Yang, A. N. Young, M. D. Wang, S. Nie, *Nat. Biotechnol.* **2007**, *26*, 83–90.
[40] T. Pellegrino, L. Manna, S. Kudera, T. Liedl, D. Koktysh, A. L. Rogach, S. Keller, J. Rädler, G. Natile, W. J. Parak, *Nano Lett.* **2004**, *4*, 703–707.
[41] C.-A. J. Lin, R. A. Sperling, J. K. Li, T.-Y. Yang, P.-Y. Li, M. Zanella, W. H. Chang, W. J. Parak, *Small* **2008**, *4*, 334–341.

[42] F. Zhang, E. Lees, F. Amin, P. RiveraGil, F. Yang, P. Mulvaney, W. J. Parak, *Small* **2011**, *7*, 3113–3127.
[43] R. Asapu, N. Claes, S. Bals, S. Denys, C. Detavernier, S. Lenaerts, S. W. Verbruggen, *Appl. Catal. B Environ.* **2017**, *200*, 31–38.
[44] A. Sánchez-Iglesias, M. Grzelczak, T. Altantzis, B. Goris, J. Perez-Juste, S. Bals, G. Van Tendeloo, S. H. Donaldson Jr, B. F. Chmelka, J. N. Israelachvili, et al., *ACS Nano* **2012**, *6*, 11059–11065.
[45] Y. Chen, D. Yang, Y. J. Yoon, X. Pang, Z. Wang, J. Jung, Y. He, Y. W. Harn, M. He, S. Zhang, et al., *J. Am. Chem. Soc.* **2017**, *139*, 12956–12967.
[46] X. Li, J. Iocozzia, Y. Chen, S. Zhao, X. Cui, W. Wang, H. Yu, S. Lin, Z. Lin, *Angew. Chem. Int. Ed.* **2018**, *57*, 2046–2070.
[47] M. N. Sanz-Ortiz, K. Sentosun, S. Bals, L. M. Liz-Marzán, *ACS Nano* **2015**, *9*, 10489–10497.
[48] J. E. Galván-Moya, T. Altantzis, K. Nelissen, F. M. Peeters, M. Grzelczak, L. M. Liz-Marzán, S. Bals, G. Van Tendeloo, *ACS Nano* **2014**, *8*, 3869–3875.
[49] C. Hanske, M. N. Sanz-Ortiz, L. M. Liz-Marzán, *Adv. Mater.* **2018**, *30*, 1707003.
[50] D. Paramelle, D. Nieves, B. Brun, R. S. Kraut, D. G. Fernig, *Adv. Healthc. Mater.* **2015**, *4*, 911–917.
[51] B. Du, X. Gu, X. Han, G. Ding, Y. Wang, D. Li, E. Wang, J. Wang, *ChemMedChem* **2017**, *12*, 1768–1775.
[52] E. Pöselt, C. Schmidtke, S. Fischer, K. Peldschus, J. Salamon, H. Kloust, H. Tran, A. Pietsch, M. Heine, G. Adam, et al., *ACS Nano* **2012**, *6*, 3346–3355.
[53] H. Kloust, C. Schmidtke, J.-P. Merkl, A. Feld, T. Schotten, U. E. A. Fittschen, M. Gehring, J. Ostermann, E. Pöselt, H. Weller, *J. Phys. Chem. C* **2013**, *117*, 23244–23250.
[54] H. Kloust, C. Schmidtke, A. Feld, T. Schotten, R. Eggers, U. E. A. Fittschen, F. Schulz, E. Pöselt, J. Ostermann, N. G. Bastús, et al., *Langmuir* **2013**, *29*, 4915–4921.
[55] I. Mekis, D. V. Talapin, A. Kornowski, M. Haase, H. Weller, *J. Phys. Chem. B* **2003**, *107*, 7454–7462.
[56] M. Rafipoor, C. Schmidtke, C. Wolter, C. Strelow, H. Weller, H. Lange, *Langmuir* **2015**, *31*, 9441–9447.
[57] J. Ostermann, J.-P. Merkl, S. Flessau, C. Wolter, A. Kornowksi, C. Schmidtke, A. Pietsch, H. Kloust, A. Feld, H. Weller, *ACS Nano* **2013**, *7*, 9156–9167.
[58] M. Henriksen-Lacey, S. Carregal-Romero, L. M. Liz-Marzán, *Bioconjug. Chem.* **2017**, *28*, 212–221.
[59] M. Mahmoudi, J. Meng, X. Xue, X. J. Liang, M. Rahman, C. Pfeiffer, R. Hartmann, P. R. Gil, B. Pelaz, W. J. Parak, et al., *Biotechnol. Adv.* **2014**, *32*, 679–692.
[60] T.-G. Iversen, T. Skotland, K. Sandvig, *Nano Today* **2011**, *6*, 176–185.
[61] C. Schmidtke, H. Kloust, N. G. Bastús, J.-P. Merkl, H. Tran, S. Flessau, A. Feld, T. Schotten, H. Weller, *Nanoscale* **2013**, *5*, 11783.
[62] N. G. Bastús, J. Comenge, V. Puntes, *Langmuir* **2011**, *27*, 11098–11105.
[63] N. G. Bastús, F. Merkoçi, J. Piella, V. Puntes, *Chem. Mater.* **2014**, *26*, 2836–2846.
[64] A. B. Serrano-Montes, D. J. de Aberasturi, J. Langer, J. J. Giner-Casares, L. Scarabelli, A. Herrero, L. M. Liz-Marzán, *Langmuir* **2015**, *31*, 9205–9213.
[65] M. G. Soliman, B. Pelaz, W. J. Parak, P. del Pino, *Chem. Mater.* **2015**, *27*, 990–997.
[66] H. Hinterwirth, S. Kappel, T. Waitz, T. Prohaska, W. Lindner, M. Lämmerhofer, *ACS Nano* **2013**, *7*, 1129–1136.
[67] D. N. Benoit, H. Zhu, M. H. Lilierose, R. A. Verm, N. Ali, A. N. Morrison, J. D. Fortner, C. Avendano, V. L. Colvin, *Anal. Chem.* **2012**, *84*, 9238–9245.
[68] J. F. Hicks, D. T. Miles, R. W. Murray, *J. Am. Chem. Soc.* **2002**, *124*, 13322–13328.
[69] C. Schmidtke, R. Eggers, R. Zierold, A. Feld, H. Kloust, C. Wolter, J. Ostermann, J.-P. Merkl, T. Schotten, K. Nielsch, et al., *Langmuir* **2014**, *30*, 11190–11196.
[70] C.-W. Wang, A. Oskooei, D. Sinton, M. G. Moffitt, *Langmuir* **2010**, *26*, 716–723.
[71] S. Bals, B. Goris, L. M. Liz-Marzán, G. Van Tendeloo, *Angew. Chem. Int. Ed.* **2014**, *53*, 10600–10610.

[72] L. Fabris, *ChemNanoMat* **2016**, *2*, 249–258.
[73] D. Steinigeweg, M. Schütz, M. Salehi, S. Schlücker, *Small* **2011**, *7*, 2406–2406.
[74] D. Paramelle, A. Sadovoy, S. Gorelik, P. Free, J. Hobley, D. G. Fernig, *Analyst* **2014**, *139*, 4855–4861.
[75] M. Fisichella, H. Dabboue, S. Bhattacharyya, M.-L. Saboungi, J.-P. Salvetat, T. Hevor, M. Guerin, *Toxicol. In Vitro* **2009**, *23*, 697–703.
[76] A. A. Stepanenko, V. V. Dmitrenko, *Gene* **2015**, *574*, 193–203.
[77] X. Ma, R. Hartmann, D. Jimenez de Aberasturi, F. Yang, S. J. H. Soenen, B. B. Manshian, J. Franz, D. Valdeperez, B. Pelaz, N. Feliu, et al., *ACS Nano* **2017**, *11*, 7807–7820.
[78] M. Akter, M. T. Sikder, M. M. Rahman, A. K. M. A. Ullah, K. F. B. Hossain, S. Banik, T. Hosokawa, T. Saito, M. Kurasaki, *J. Adv. Res.* **2018**, *9*, 1–16.
[79] D. Wang, M. Hermes, R. Kotni, Y. Wu, N. Tasios, Y. Liu, B. de Nijs, E. B. van der Wee, C. B. Murray, M. Dijkstra, et al., *Nat. Commun.* **2018**, *9*, 2228.
[80] L. Scarabelli, A. Sánchez-Iglesias, J. Pérez-Juste, L. M. Liz-Marzán, *J. Phys. Chem. Lett.* **2015**, *6*, 4270–4279.
[81] B. Mir-Simon, J. Morla-Folch, P. Gisbert-Quilis, N. Pazos-Perez, H. Xie, N. G. Bastús, V. Puntes, R. A. Alvarez-Puebla, L. Guerrini, *J. Opt.* **2015**, *17*, 114012.
[82] R. Thiermann, W. Mueller, A. Montesinos-Castellanos, D. Metzke, P. Löb, V. Hessel, M. Maskos, *Polymer* **2012**, *53*, 2205–2210.

ADVANCED FUNCTIONAL MATERIALS

Supporting Information

for *Adv. Funct. Mater.,* DOI: 10.1002/adfm.201809071

Encapsulation of Noble Metal Nanoparticles through Seeded Emulsion Polymerization as Highly Stable Plasmonic Systems

Leonardo Scarabelli, Marius Schumacher, DorletaJimenez de Aberasturi, Jan-Philip Merkl, Malou Henriksen-Lacey, ThaisMilagres de Oliveira, Marcus Janschel, Christian Schmidtke, Sara Bals, Horst Weller,* and Luis M. Liz-Marzán**

Supporting Information

Encapsulation of Noble Metal Nanoparticles through Seeded Emulsion Polymerization as Highly Stable Plasmonic Systems

Leonardo Scarabelli[1,2,†,*], Marius Schumacher[3,†], Dorleta Jimenez de Aberasturi[1], Jan-Philip Merkl[3], Malou Henriksen-Lacey[1], Thais Milagres de Oliveira[4], Marcus Janschel[3], Christian Schmidtke[3], Sara Bals[4], Horst Weller[3,*], and Luis M. Liz-Marzán[1,5*]

[1]CIC biomaGUNE and CIBER-BBN, Paseo de Miramón 182, 20014 Donostia-San Sebastián, Spain
[2]Department of Chemistry & Biochemistry, University of California Los Angeles, Los Angeles, California 90095 USA
[3]Institute of Physical Chemistry, University of Hamburg, 20146 Hamburg, Germany
[4]Electron Microscopy for Materials Science (EMAT), University of Antwerp, Groenenborgerlaan 171, 2020 Antwerp, Belgium
[5]Ikerbasque, Basque Foundation for Science, 48013 Bilbao, Spain

[†] These authors contributed equally
*Corresponding authors: lscarabelli@ucla.edu (LS); weller@chemie.uni-hamburg.de (HW); llizmarzan@cicbiomagune.es (LMLM)

1. Phase-transfer of citrate-stabilized gold nanoparticles in nonpolar solvent.

The absorption of the aqueous and the organic phase was observed via UV/Vis-spectroscopy at certain points of time to trace the progress of the transfer. The time measurement starts from the beginning of the emulsification of the two phases through vigorous stirring with a magnetic stir bar (see **Figure S1**). The higher the intensity of the characteristic gold nanoparticle absorbance in the organic phase is, the higher the progress of the transfer. The intention of these kinetic measurements is to investigate the most effective ligand concentration.

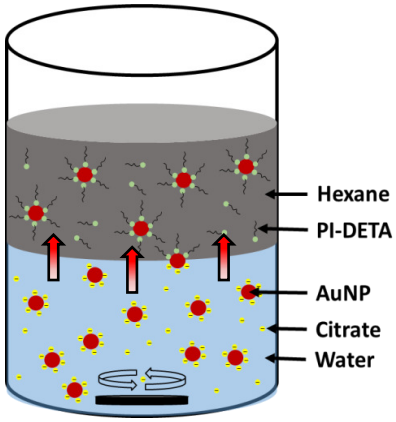

Figure S1: Schematic representation of the phase transfer of citrate-stabilized gold nanoparticles from water to hexane using PI-DETA.

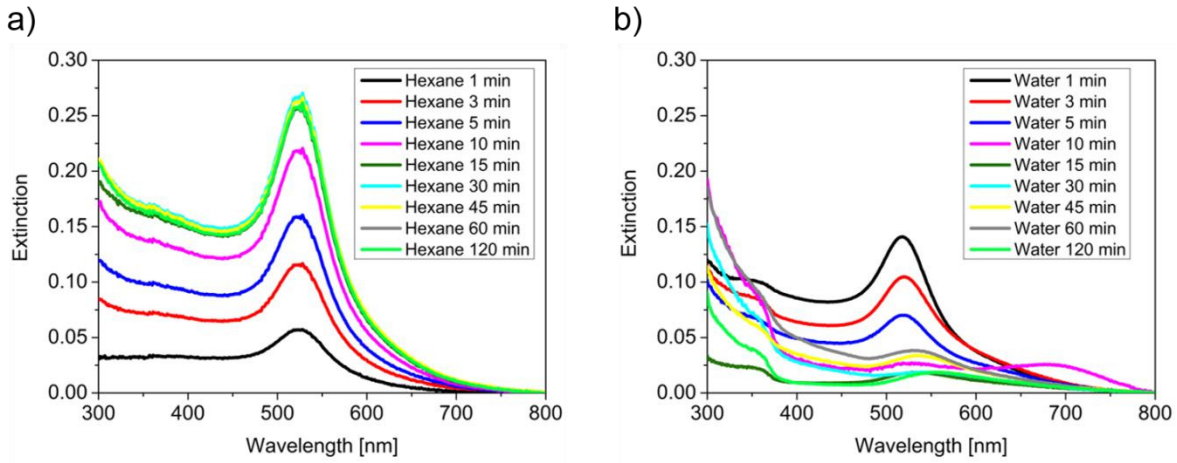

Figure S2. UV/Vis spectra of the organic **(a)** and the corresponding aqueous phase **(b)** during the phase transfer of gold nanoparticles with approx. 3000 eqv. of PI-DETA at certain points of emulsification time.

Since the absorbance at 400 nm is proportional to the concentration of gold nanoparticles, it can be plotted against the time (**Figure S3**).[1]

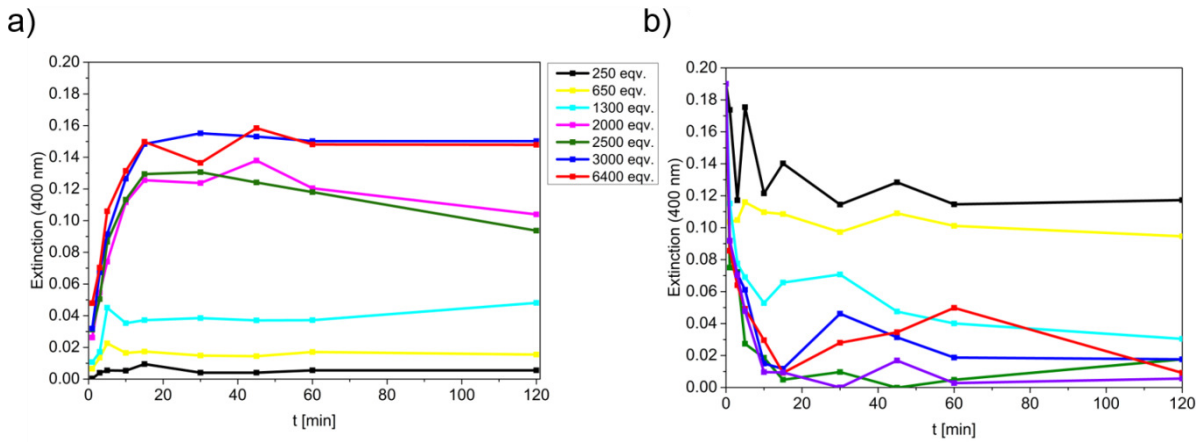

Figure S3. **(a)** Plot of the extinction at 400 nm of the hexane phase against the time during the gold nanoparticle phase transfer with selected equivalents of PI-DETA. **(b)** Plot of the absorbance at 400 nm of the associated aqueous phase against the time during the phase transfer.

Figure S3 a) displays that the concentration of gold nanoparticles in hexane after 2 hours of emulsification is low when less than 2000 eqv. are used. The addition of more than 2500 ligands per gold nanoparticle leads to a quick, almost quantitative transfer of the colloid into hexane. With 3000 ligands per nanoparticle the transfer is completed after 15 minutes, when the extinction at 400 nm in hexane reached saturation. The surface area of the used gold nanoparticles is: $A = \pi d^2 = \pi \cdot (18\ \text{nm})^2 = 1018\ \text{nm}^2 \approx 1000\ \text{nm}^2$. Accordingly, an efficient phase transfer is possible, if three PI-DETA ligands per square nanometer of gold surface (here 3000 eqv.) are available. Helmut Hinterwirth et al. quantified the surface coverage of different sized thiol ligands of self-assembled monolayers on different sized gold nanoparticles by inductively coupled plasma-mass spectrometry,[2] and a ligand length-dependent surface coverage was found. For instance, thiolated PEO ligands with the length of 2.1 nm ($\approx$ 300 $g \cdot mol^{-1}$) and 3.5 nm ($\approx$ 500 $g \cdot mol^{-1}$) exhibit a surface coverage of 4.9 ± 0.27 and of 4.3 ± 0.45 ligands per square nanometer of gold surface. In another work, Denise N. Benoit et al.

measured the surface coverage of Gold nanoparticles in solution by analytical ultracentrifugation and total organic carbon analysis.[3] The average surface coverage of gold nanoparticles (d ≈ 10 nm) with thiolated PEO ligands of 1000 g·mol^{-1} and 2000 g·mol^{-1} were found to be 4.12 ± 0.70 ligands/nm^2 and 2.50 ± 0.12 ligands/nm^2. In our case, approximately 3 ligands per square nanometer for 1300 g·mol^{-1} PI-DETA correspond to the packing densities and the given tendencies from the literature for other linear polymer ligands. In addition, 2000 eqv. or 2 ligands/nm² are required for an effective phase transfer with 2500 g·mol^{-1} PI-DETA, which also agrees with the literature tendencies.

1.1 Aggregation during Phase Transfer

The relative aggregation parameter AP of the Gold nanoparticles over the time of both phases was calculated from the UV/Vis spectra using the following equation:

$$AP = \frac{\int_{600}^{800} A(\lambda)\, d\lambda}{\int_{500}^{600} A(\lambda)\, d\lambda}$$

Where the Intensity A(λ) represents the absorbance between 500 - 600 nm and 600 - 800 nm at different points in time.

The plasmon coupling range (600-800 nm) was chosen according to previous literature.[4,5] The non-aggregated plasmon range (500-600 nm) was chosen around the position of the localized surface plasmon resonance band of non-aggregated ~20 nm sized gold nanoparticles.

In other words, AP is a relative parameter for the degree of gold nanoparticle aggregation. **Figure S4.** a) shows that the relative AP in hexane is not constant at a ratio of less than 2500 PI-DETA ligands per Gold nanoparticle (≈ 2.5 PI-DETA/nm^2), while the AP for ~3 PI-DETA/nm^2 in hexane is roughly constant.

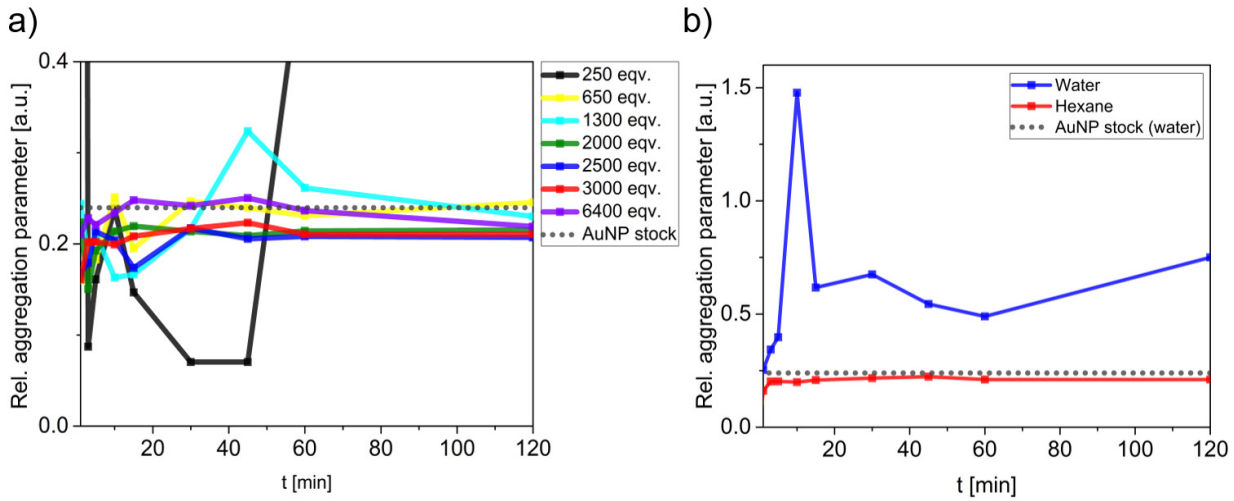

Figure S4. Plot of the AP of selected phase transfers. **(a)** Relative Aggregation parameter of selected gold nanoparticles samples in hexane over the time: 250 eqv. (black), 650 eqv. (yellow), 1300 eqv. (cyan), 2000 eqv. (green), 2500 eqv. (blue), 3000 eqv. (red), 6400 eqv. (purple) and the aqueous Gold nanoparticle stock dispersion (grey dotted line). **(b)** AP of Gold nanoparticles with 3000 eqv. PI-DETA over the time in hexane (red) and water (blue) in comparison to the AP of the aqueous Gold nanoparticle stock dispersion (grey dotted line).

1.2 Phase Transfer with several ligands at different pH values

The phase transfer was also conducted with other ligands at different pH values. The results are summarized in **Table T1**.

Table T1. The ligands that were used for the phase transfer with the respective pH scale, the success of the transfer of 18 nm diameter gold nanoparticles and the time until the concentration in hexane reached saturation (c(sat)) are presented. The data is referred to a transfer with 3000 or more eqv. of the respective ligand. PI-DTC = polyisoprene dithiocarbamate.

	pH scale	**Transfer**	**Time to c(sat) [min]**
PI-DETA	5.5	Observed	~ 15
	11	Insufficient	-
PI-DTC	5.5	Observed	~ 40
	11	Insufficient	-
Oleylamine	5.5, 11	Insufficient	-
1-Octanethiol	5.5, 11	-	-
1-Octadecanethiol	5.5,11	-	-

In the case of PI-DETA the phase transfer worked well when the amines of the anchoring group are likely protonated (pH of the aqueous phase = 5.5) although they have to be deprotonated to bind to the gold surface over the lone pair electrons.[6] Since the transfer worked adequately in the acid pH range, it can be concluded that the result of the transfer depends, among other factors like chain lengths, on the charge of the anchoring groups.

1.3 Phase Transfer scalability

If the pH is neutral or slightly acidic (pH 5.5 – 7), the surface area A and the ideal PI-DETA surface coverage (ρ_A [nm^{-2}]; M_W dependent) is known, the concentration c(PI-DETA) and the solvent volumes can be scaled using the following equation:

$$c(\text{PI-DETA}) = \frac{c(\text{NPs}) \cdot V(\text{NPs}_{\text{water}}) \cdot A(\text{NP}) \cdot \rho_A}{V(\text{hexane})}$$

Based on this formula, a phase transfer with a 600 mL aqueous gold nanoparticle dispersion (~ 7 nM) and 400 mL hexane has been successfully performed.

Long-term colloidal stability of Gold nanoparticles@PI-DETA in hexane

The gold nanoparticles show high stability and can be stored at 4°C and cover from light for at least 6 months without losing their plasmonic and colloidal properties (**Figure S5**.).

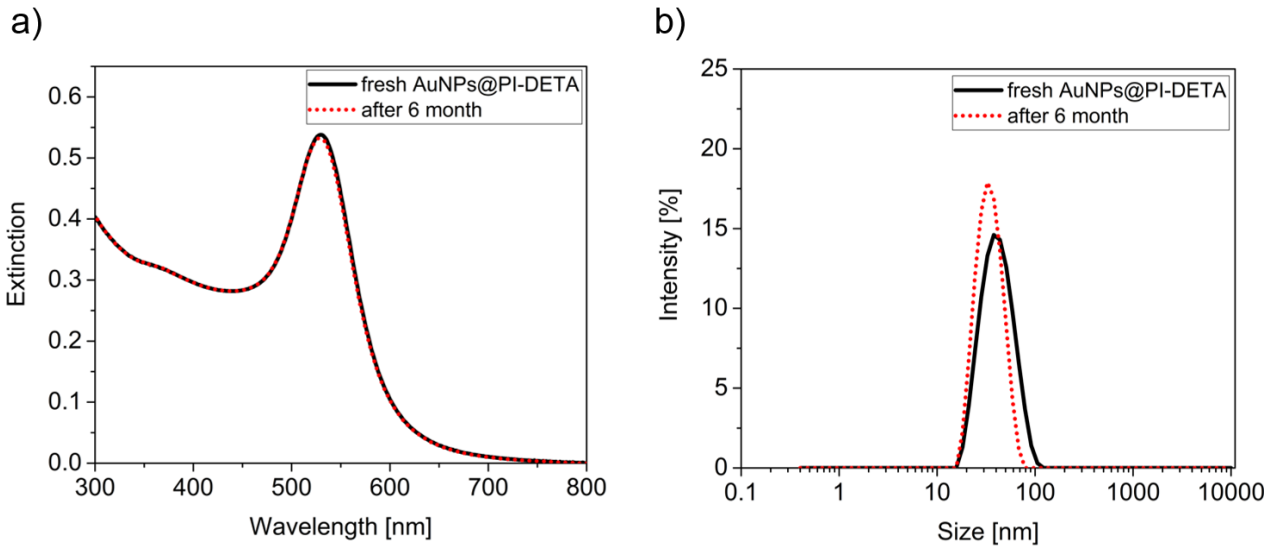

Figure S5. (a) UV-Vis spectra of gold nanoparticles@PI-DETA in hexane. **(b)** DLS study of gold nanoparticles@PI-DETA in hexane. Freshly prepared gold nanoparticles@PI-DETA in hexane with 3000 eqv. PI-DETA (black line), the same dispersion after 6 month storage (dotted red line).

2. NP cluster size

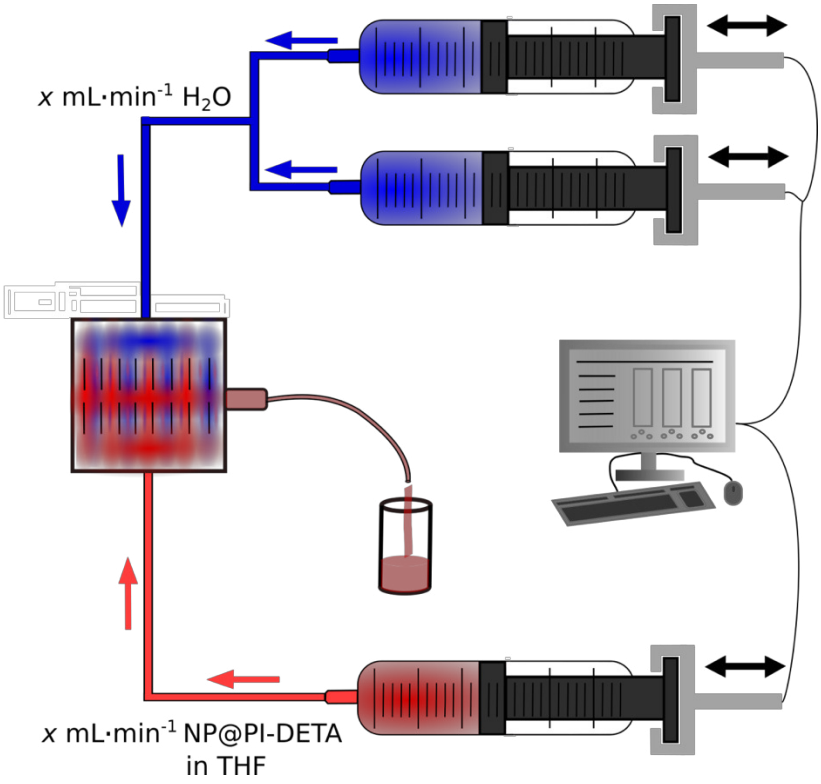

Figure S6. Schematic sketch of the mixing setup for the cluster formation.

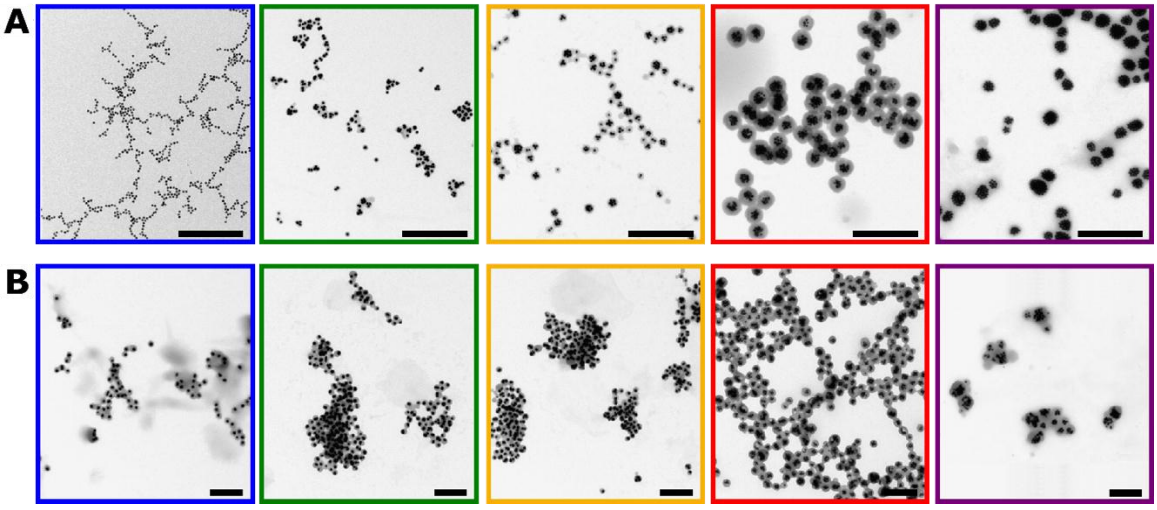

Figure S7. Low magnification TEM images (**A, B**) of single and clustered encapsulated gold- **(A)** and silver **(B)** nanoparticles, prepared with different molar ratios of PI-b-PEO relative to the constant amount of the PI-DETA ligands. PI-b-PEO:PI-DETA ratio: 1:2.5 (**blue**), 1:10 (**green**), 1:20 (**yellow**), 1:30 (**red**), 1:60 (**purple**). Scale bars = 500 nm.

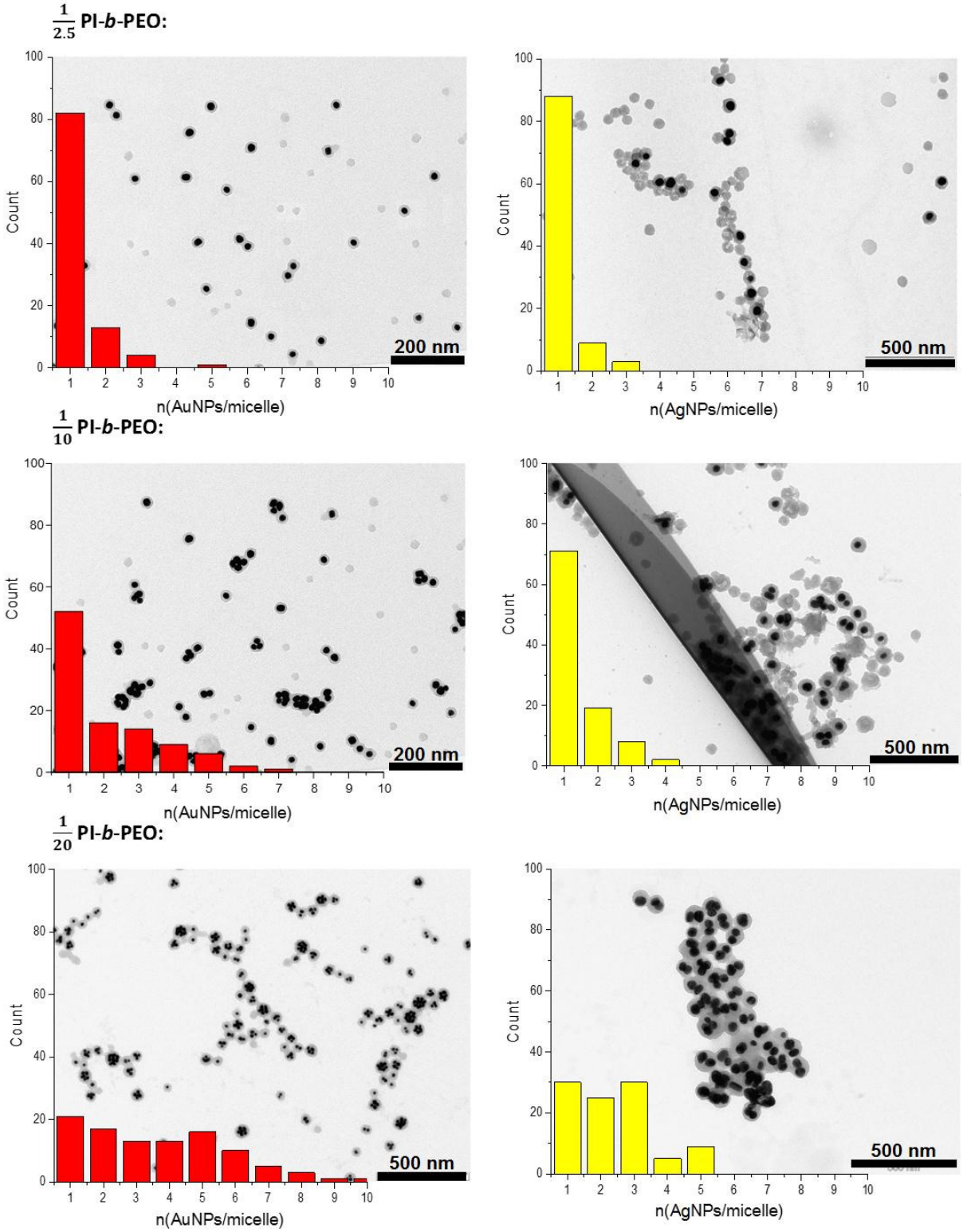

Figure S8. Gold (right) and Silver (left) nanoparticle cluster size distribution from **Table 2.** The TEM images were prepared without purification.

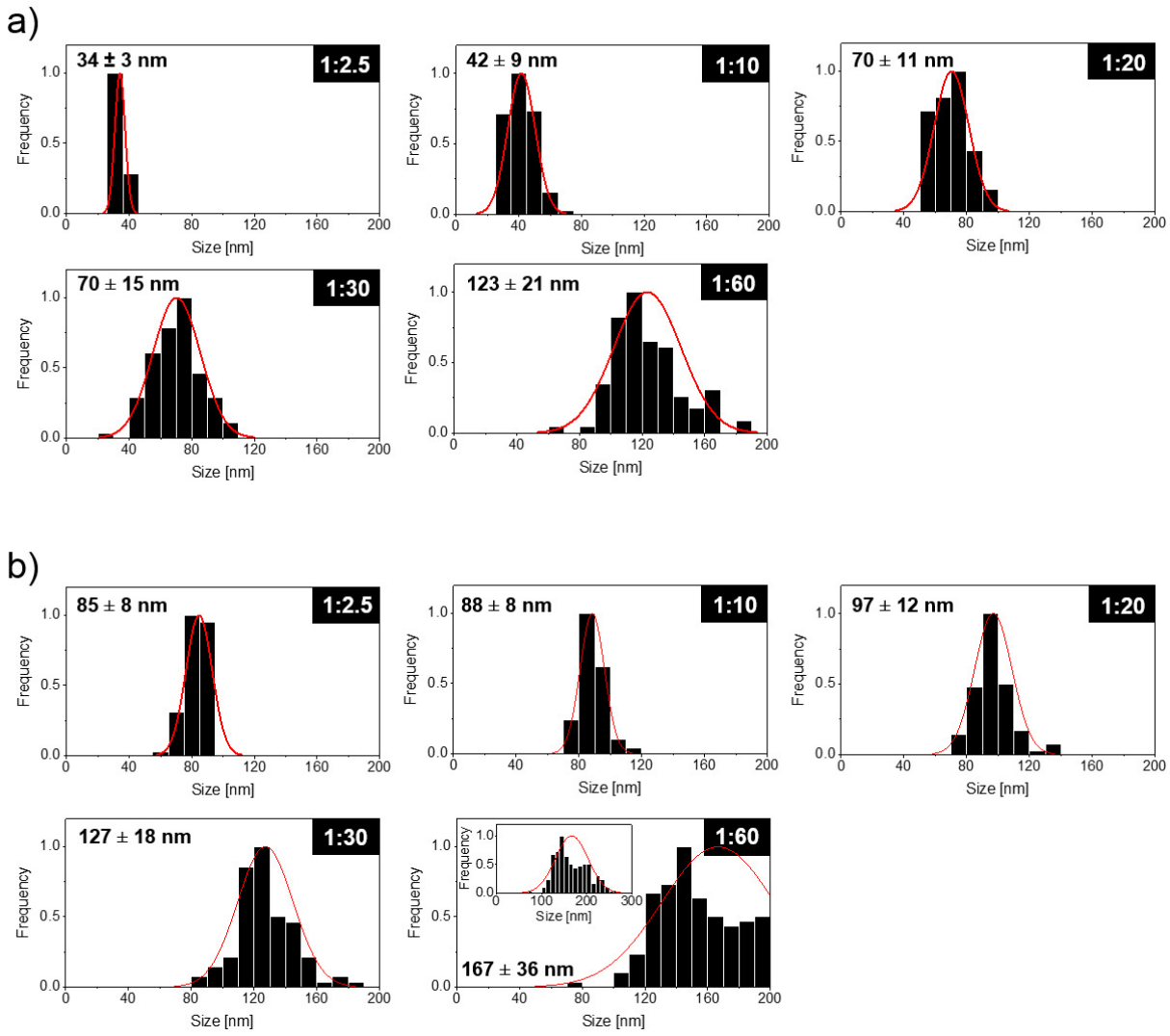

Figure S9. Gold **(a)** and Silver **(b)** nanoparticle cluster size histograms distribution. At least 100 micelles were counted each.

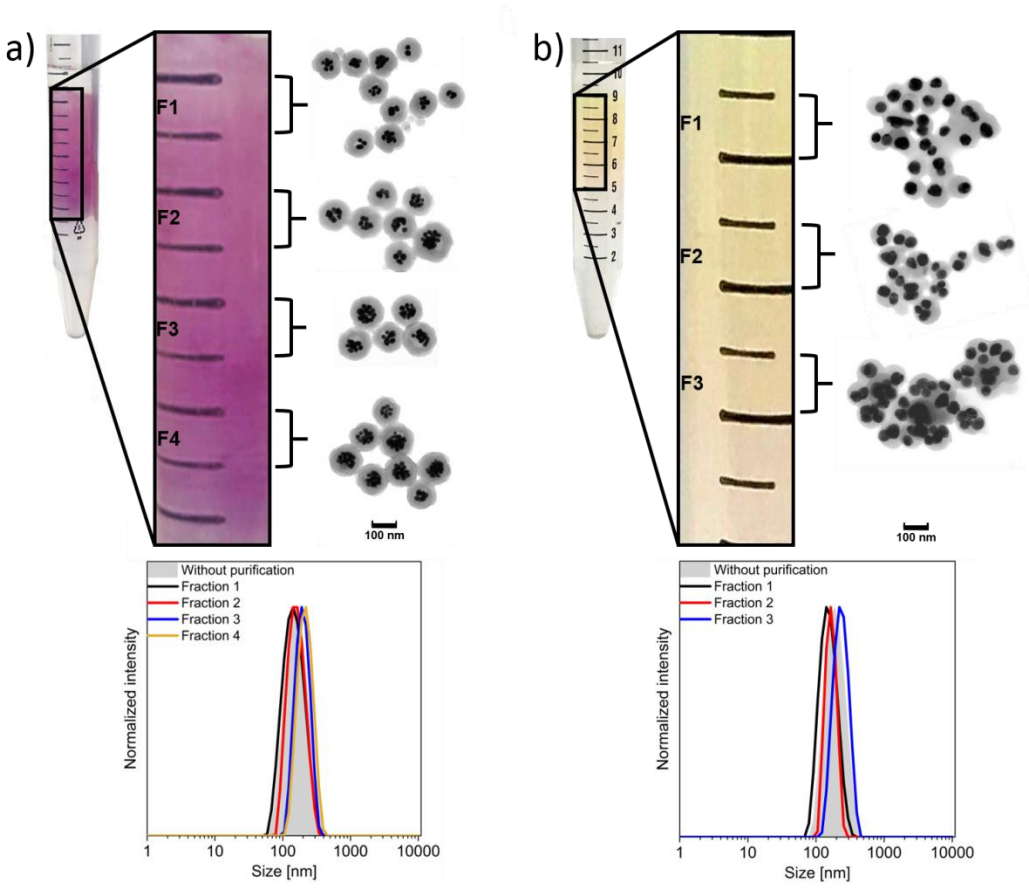

Figure S10. Purification and size-separation of encapsulated gold **(a)** and silver **(b)** nanoparticle clusters by continuous density gradient centrifugation and the corresponding DLS measurements of each fraction. The TEM images correspond to the marked fractions. Both samples were obtained with a PI-b-PEO to PI-DETA ratio of 1:20.

3. Stability tests

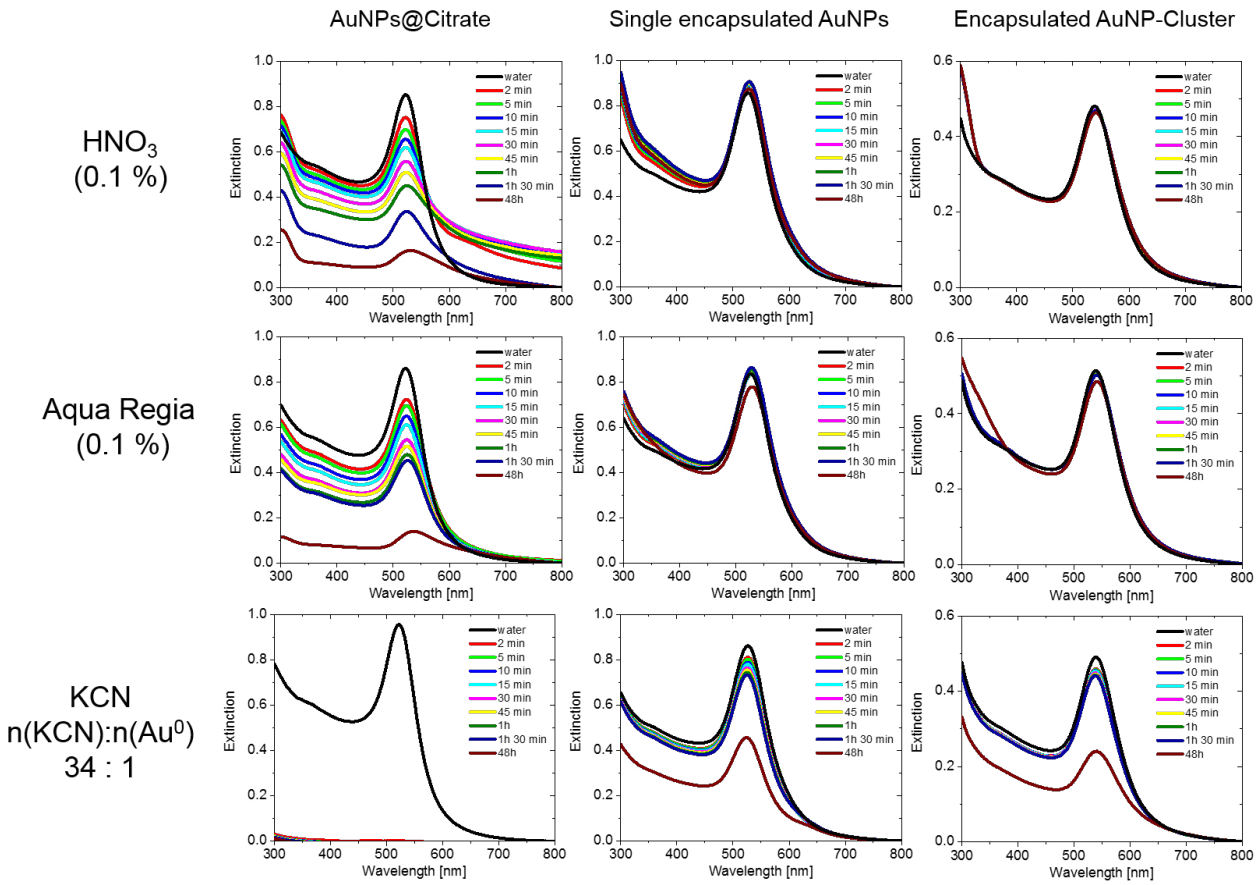

Figure S11. UV-Vis spectra of citrate capped, single and clustered encapsulated gold nanoparticles in different aqueous media (0.1 % HNO_3, 0.1 % acqua regia and a KCN-solution (34:1, n(KCN):n(Au^0)) at different exposure times. The columns refer to the respective gold nanoparticle systems and the rows refer to the respective media.

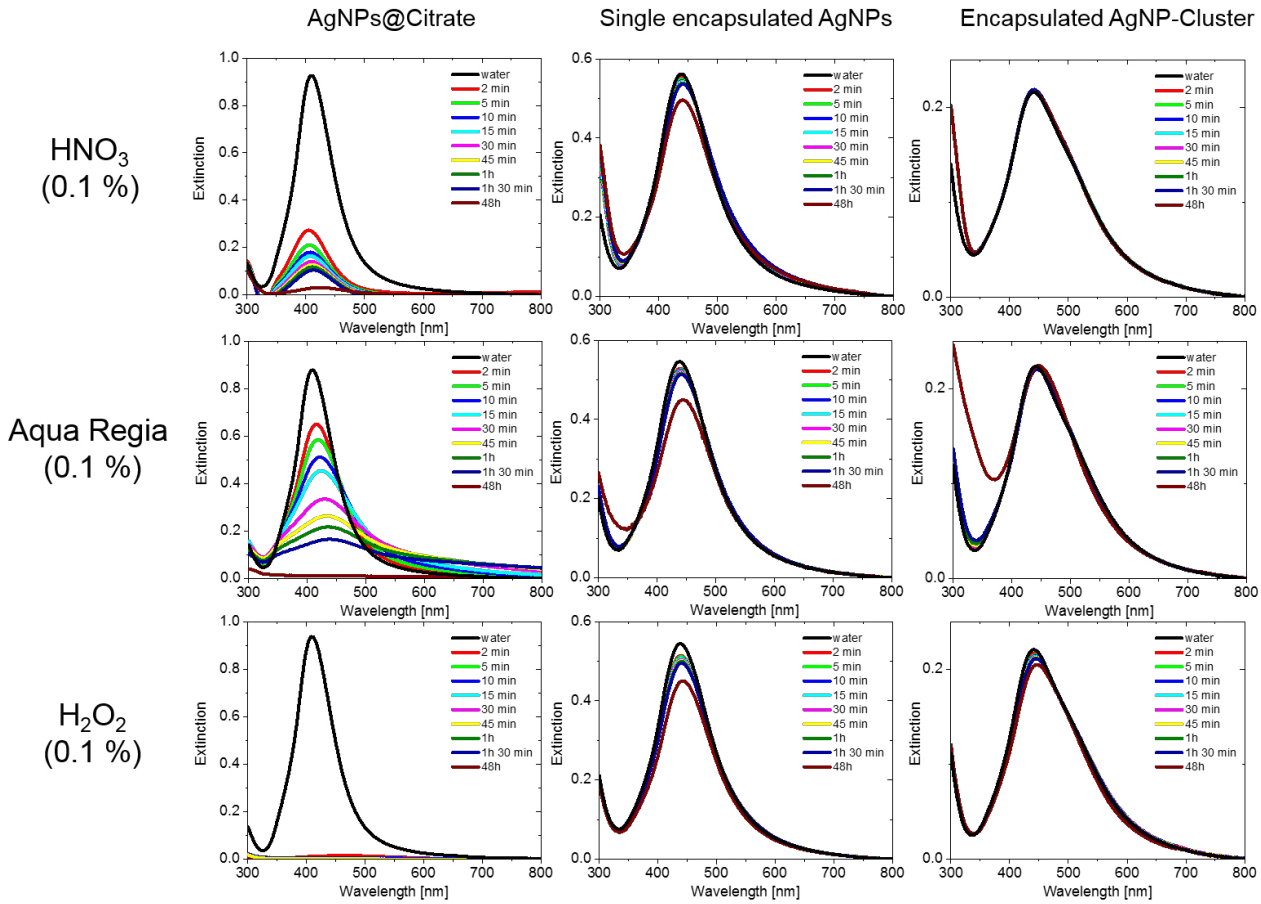

Figure S12. UV-Vis spectra of citrate capped, single and clustered encapsulated silver nanoparticles in different aqueous media (0.1 % HNO_3, 0.1 % acqua regia and 0.1 % H_2O_2) at different exposure times. The columns refer to the respective silver nanoparticle systems and the rows refer to the respective media.

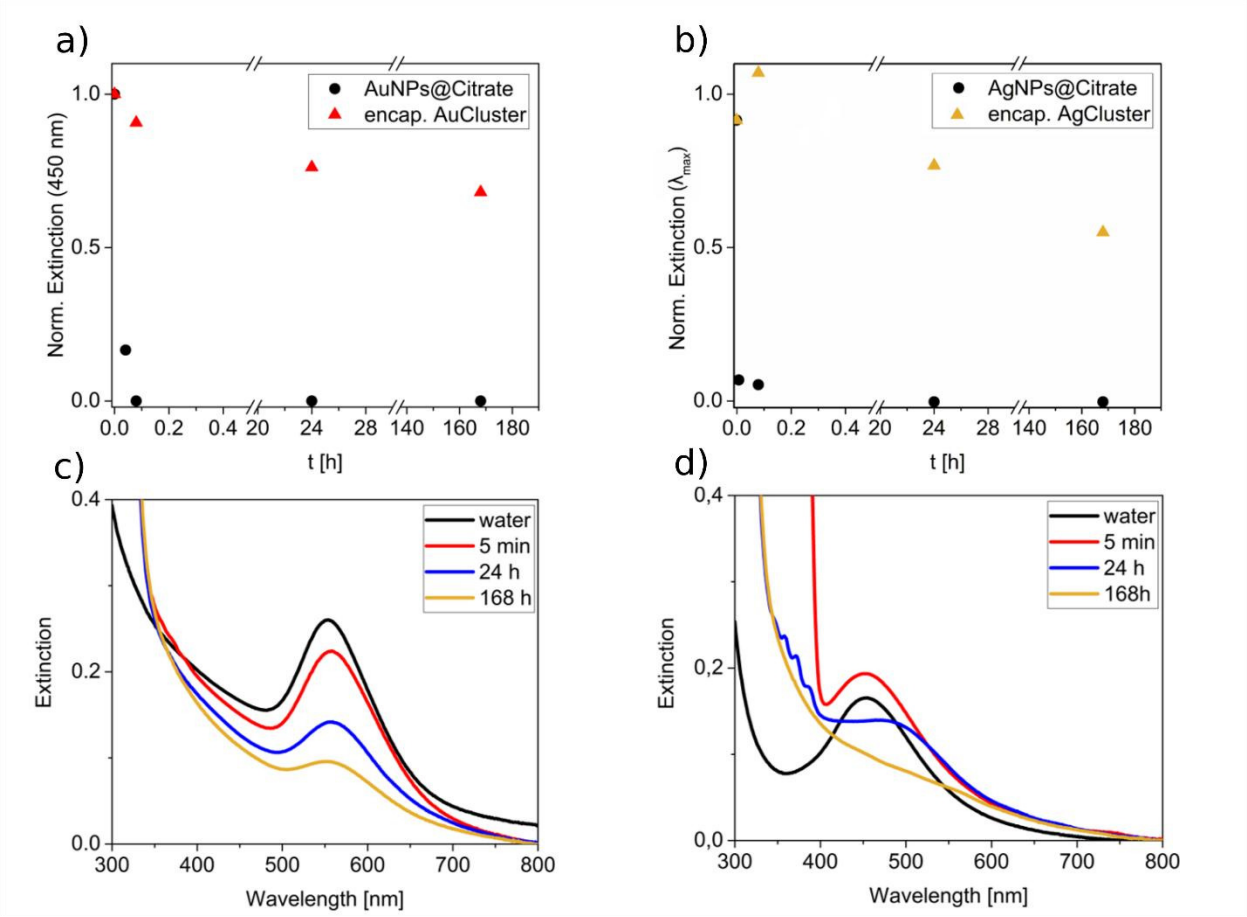

Figure S13. **(a)** UV-Vis stability studies of citrate capped gold nanoparticles (black circles), encapsulated gold nanoparticles (red triangles, 1/20 PI-b-PEO) in 10% aqua regia with the absorbance at 450 nm plotted against the exposure time.[7] We could not use the absorbance at 400 nm as in the rest of the manuscript due to the strong interference from aqua regia at that wavelength. **(b)** UV-Vis stability studies of citrate capped silver nanoparticles (black circles), encapsulated silver nanoparticles (yellow triangles, 1/20 PI-b-PEO) in 10% aqua regia with the absorbance at the band maxima plotted vs. exposure time. (**c-d**) UV-Vis spectra of gold (**c**) and silver (**d**) clusters over time in 10% aqua regia solution.

4. Cell viability

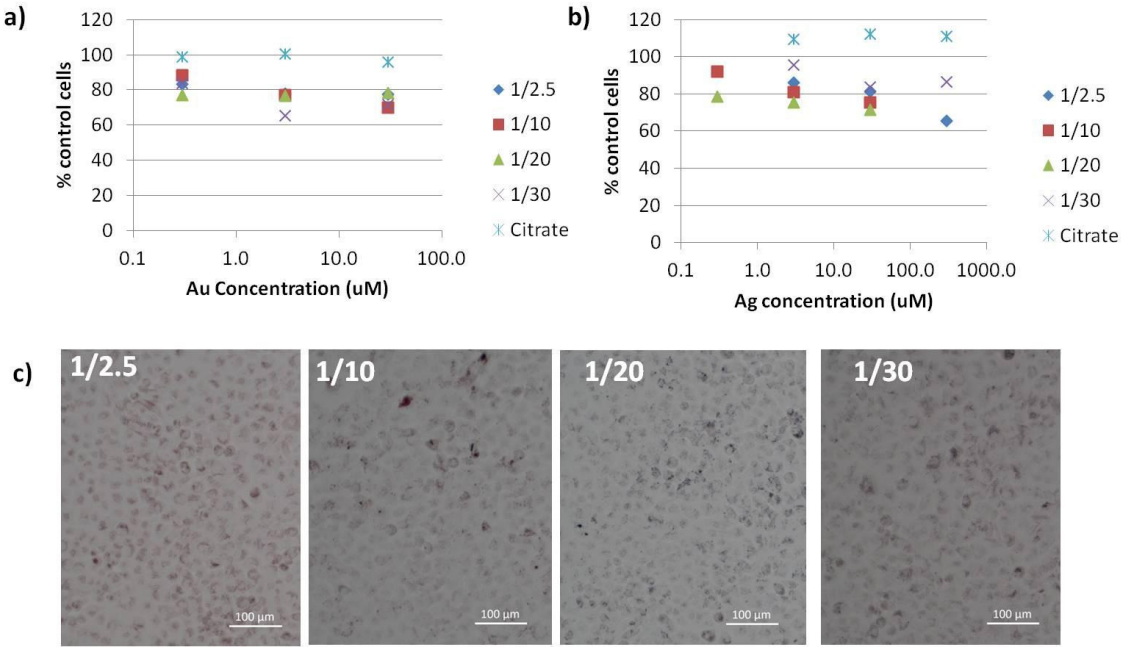

Figure S14. Cell viability of A549 cells with clusters of different sizes prepared with different molar ratios of PI-b-PEG relative to the constant amount of the PI-DETA ligands (~ 3000 eqv. per nanoparticle), expressed as the % of control cells, measured with the MTT assay after exposure to gold **(a)** and silver **(b)** nanoparticles. **c**) Light microscope images of A549 cells incubated with gold nanoparticles (all at 30uM).

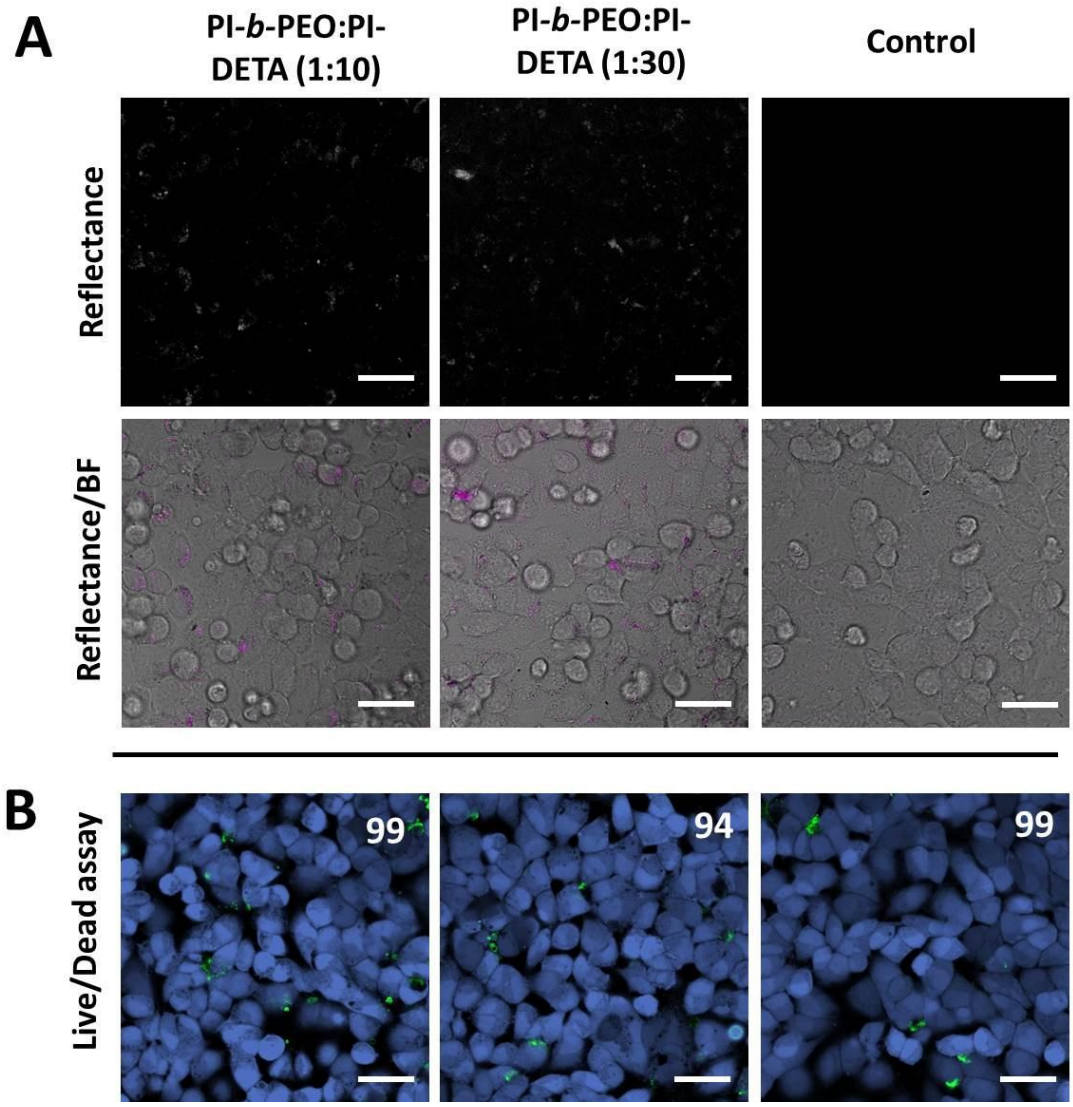

Figure S15. A: Reflectance confocal mages of HeLa cells exposed to PI-b-PEO:PI-DETA NPs at 1:10 and 1:30 ratios, for 48 h, at a final concentration of 30 uM. Images of nanoparticle reflectance in original black-white (**top**) and combined false-coloured pink with transmission (**bottom**) are shown. **B:** Live/dead staining of the same NP conditions described above. Cells were stained with three fluorophores marking live (**blue**), apoptotic (**green**) and necrotic (**red**) cells. Note there are no necrotic (**red**) cells present, and the presence of apoptotic cells or fragments (**green**) are very few and similar in control and nanoparticle incubated samples. The number of live cells per field of view were counted and the mean of 2 images is shown in the top right corner. Scale bar: 40 µm.

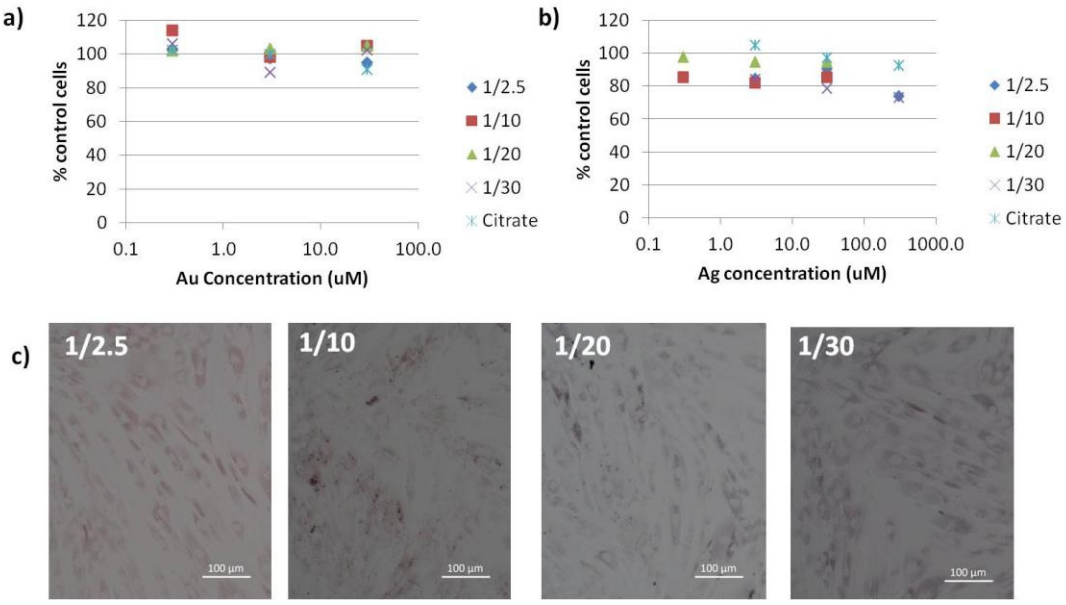

Figure S16. Cell viability of HDF cells with clusters of different sizes prepared with different molar ratios of PI-b-PEG relative to the constant amount of the PI-DETA ligands (~ 3000 eqv. per nanoparticle), expressed as the % of control cells, measured with the MTT assay after exposure to gold **(a)** and silver **(b)** nanoparticles. **C**) Light microscope images of HDF cells incubated with gold nanoparticles (all at 30uM).

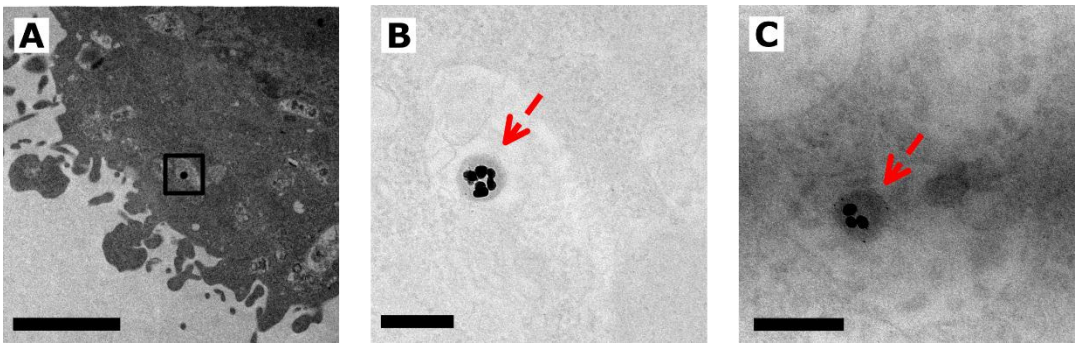

Figure S17. **A-C:** Representative TEM images at different magnifications showing the cellular uptake by HeLa cells of encapsulated silver clusters with PI-b-PEO:PI-DETA ratios of 1:30. **B,C:** High magnification images of an uptaken cluster, where the polymeric shell can be distinguished (**red arrows**), confirming the stability of clusters after internalization inside endosomal vesicles. Scale bars: **A:** 2 µm; **B, C:** 200 nm.

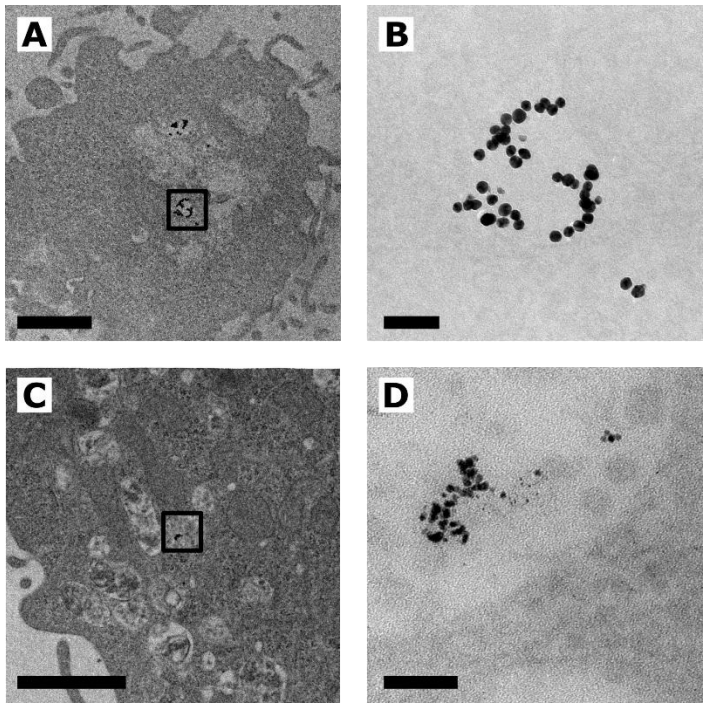

Figure S18. **A-D:** Representative TEM images at different magnifications showing the cellular uptake by HeLa cells, of gold (**A,B**) and silver (**C,D**) citrate nanoparticles. In this case the protective polymeric shell is not present, and silver capped nanoparticles show clear signs of degradation (**D**). Scale bars: **A:** 1 μm; **B-D:** 50 nm.

References:

[1] L. Scarabelli, A. Sánchez-Iglesias, J. Pérez-Juste, L. M. Liz-Marzán, J. Phys. Chem. Lett. **2015**, 6, 4270–4279.
[2] H. Hinterwirth, S. Kappel, T. Waitz, T. Prohaska, W. Lindner, M. Lämmerhofer, ACS Nano **2013**, 7, 1129–1136.
[3] D. N. Benoit, H. Zhu, M. H. Lilierose, R. A. Verm, N. Ali, A. N. Morrison, J. D. Fortner, C. Avendano, V. L. Colvin, Anal. Chem. **2012**, 84, 9238–9245.
[4] C. S. Weisbecker, M. V. Merritt, G. M. Whitesides, Langmuir **1996**, 12, 3763–3772.
[5] A. Kohut, A. Voronov, W. Peukert, Part. Part. Syst. Charact. **2005**, 22, 329–335.
[6] F. Chen, X. Li, J. Hihath, Z. Huang, N. Tao, J. Am. Chem. Soc. **2006**, 128, 15874–15881.
[7] W. Haiss, N. T. K. Thanh, J. Aveyard, D. G. Fernig, Anal. Chem. **2007**, 79, 4215–4221.